ARMY RESEARCH LABORATORY

Multiscale Modeling of Non-crystalline Ceramics (Glass) (FY11)

by George A. Gazonas, James W. McCauley, Iskander G. Batyrev, Richard C. Becker, Sergei Izvekov, Parimal Patel, Betsy M. Rice, Brian E. Schuster, N. Scott Weingarten, and Raymond A. Wildman

ARL-MR-0802 **January 2012**

NOTICES

Disclaimers

The findings in this report are not to be construed as an official Department of the Army position unless so designated by other authorized documents.

Citation of manufacturer's or trade names does not constitute an official endorsement or approval of the use thereof.

Destroy this report when it is no longer needed. Do not return it to the originator.

Army Research Laboratory

Aberdeen Proving Ground, MD 21005-5066

ARL-MR-0802 **January 2012**

Multiscale Modeling of Non-crystalline Ceramics (Glass) (FY11)

George A. Gazonas, James W. McCauley, Iskander G. Batyrev, Richard C. Becker, Sergei Izvekov, Parimal Patel, Betsy M. Rice, Brian E. Schuster, N. Scott Weingarten, and Raymond A. Wildman

Weapons and Materials Research Directorate, ARL

REPORT DOCUMENTATION PAGE	Form Approved OMB No. 0704-0188

1. REPORT DATE *(DD-MM-YYYY)*	2. REPORT TYPE	3. DATES COVERED (From - To)
January 2012	DSI	November 2010-November 2011

4. TITLE AND SUBTITLE
Multiscale Modeling of Non-crystalline Ceramics (Glass) (FY11)

5a. CONTRACT NUMBER

5b. GRANT NUMBER

5c. PROGRAM ELEMENT NUMBER

6. AUTHOR(S)
George A. Gazonas, James W. McCauley, Iskander G. Batyrev, Richard C. Becker, Sergei Izvekov, Parimal Patel, Betsy M. Rice, Brian E. Schuster, N. Scott Weingarten, Raymond A. Wildman

5d. PROJECT NUMBER
AH84

5e. TASK NUMBER

5f. WORK UNIT NUMBER

7. PERFORMING ORGANIZATION NAME(S) AND ADDRESS(ES)
U.S. Army Research Laboratory
ATTN: RDRL-WMM-B
Aberdeen Proving Ground, MD 21005-5069

8. PERFORMING ORGANIZATION REPORT NUMBER
ARL-MR-0802

9. SPONSORING/MONITORING AGENCY NAME(S) AND ADDRESS(ES)

10. SPONSOR/MONITOR'S ACRONYM(S)

11. SPONSOR/MONITOR'S REPORT NUMBER(S)

12. DISTRIBUTION/AVAILABILITY STATEMENT
Approved for public release; distribution is unlimited.

13. SUPPLEMENTARY NOTES
primary author's email: <george.a.gazonas.civ@mail.mil>

14. ABSTRACT
This second-year progress report describes an ongoing program on the multiscale modeling of noncrystalline ceramics (glass) funded from the Director's Strategic Initiatives (DSIs) in support of the U.S. Army Research Laboratory's (ARL) Strategic Research Initiatives. The long-term research goal of the program is to develop a concurrent multiscale computational finite element code for optimizing or enhancing the performance of various glasses against shaped-charge jets; the initial work focuses on pure fused-silica (a-SiO_2), and chemically varied a-SiO_2 materials. As such, this objective falls squarely within the purview of the Weapons and Materials Research Directorate, since multiscale models are constitutive models (specific to a particular material) wherein time evolving short and intermediate range atomic structure, order, and microcrack initiation and growth, are fully coupled to the macroscale, a phenomenon that cannot be modeled or accounted for using classical homogenization methods. A more immediate research objective is to understand why certain chemically substituted a-SiO_2 materials exhibit enhanced performance in the defeat of shaped-charge jets and other ballistic threats.

15. SUBJECT TERMS multiscale modeling; fused silica; amorphous quartz; molecular dynamics; quantum mechanics; shaped charge jet; Director's Strategic Initiative (DSI)

16. SECURITY CLASSIFICATION OF:			17. LIMITATION OF ABSTRACT	18. NUMBER OF PAGES	19a. NAME OF RESPONSIBLE PERSON
a. REPORT	b. ABSTRACT	c. THIS PAGE			George A. Gazonas
Unclassified	Unclassified	Unclassified	UU	68	19b. TELEPHONE NUMBER (*Include area code*) 410-306-0863

Contents

List of Figures

List of Tables

1. Introduction

Non-crystalline (amorphous) ceramics or ceramic glasses are used in a variety of vital Army personnel, ground, and air vehicle applications that require transparent armor—it is ubiquitous in tactical vehicular windshields and side windows. Ceramic glass is inexpensive and is formable into large, flat plate and curved shapes. For many years it has been known that the properties of glass can be modified and enhanced through compositional modification, chemical strengthening, annealing, and process control of melt cooling. Glass ceramics, the controlled crystallization of nano-sized single crystals in a glass matrix, offer another avenue for designed and enhanced property modifications for transparent and opaque material applications. In addition, certain glass formulations have been shown to exhibit enhanced performance against shaped-charge jets (SCJs) (figure 1) and other ballistic threats, but it is not understood why. This is in part due to various short- and longer-range atomic structural characteristics including atomic free volumes, cation coordinations, bridging and non-bridging oxygen (O) atoms, bonding energies, and nanoscale order characteristics (short and longer range) that are difficult or impossible to quantify experimentally for ceramic glass.

In contrast, crystalline ceramics like silicon carbide (SiC), aluminum oxynitride ($AlON$), and others have easily characterizable microstructures/mesostructures, which consist of assemblies of individual single-crystal grains. Ceramic glasses, on the other hand, do not have a conventional micro- or mesostructure, as it is understood for crystalline ceramics. However, there are microstructural-scale variations in ceramic glass that may include density variations from atomic free volume variations or microporosity, size of local atomic order, defects (inclusions, large pores, etc.), and others yet to be determined.

The interaction of a stress/shock wave from a dynamic impact involves many structural changes not easily characterized by conventional equations of state and can involve reversible and irreversible densification and changes in bulk short-range order structures comparable to phase changes in crystalline ceramics. For example, in simple Hertzian indentation testing, a wide range of plastic or inelastic deformation mechanisms have been observed in a variety of glasses. Multiscale computational design methodologies (figure 2), for this class of materials will, nevertheless, require quantitative and possibly statistically based descriptions of the mesoscale, although current efforts to develop such models have fallen far short of this goal.

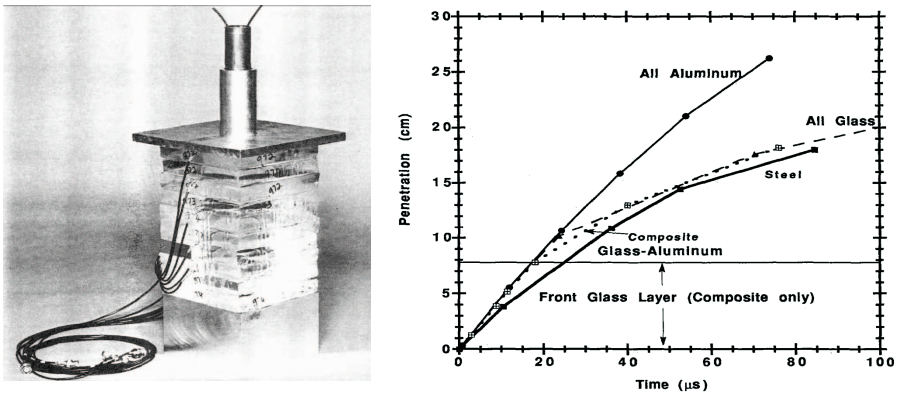

(a) (b)

Figure 1. Enhanced performance of SCJs into glass (a) test configuration for glass targets, and (b) penetration vs. time for several targets, after Moran et al. (*1*).

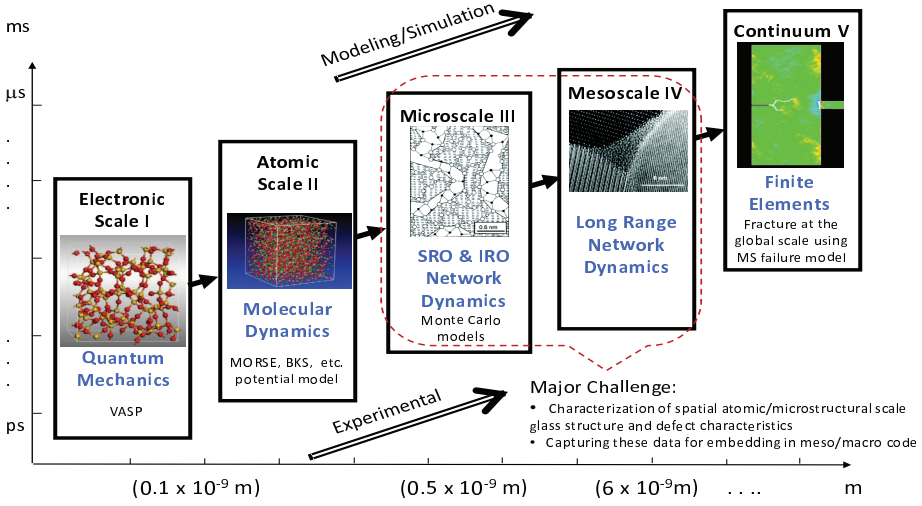

Figure 2. A multiscale model for non-crystalline ceramics (glass).

Our specific long-term research goals are threefold:

1. Develop molecular dynamics (MD) process models for a series of chemically substituted amorphous silica (a-SiO_2 or fused silica) materials for the prediction of glass elastic properties assuming completely uniform glass "mesostructures." If successful, such models will enable ab initio prediction of structure-property relations in glass that will be validated with experimentally determined elastic properties.

2. Extend the MD models to study densification of chemically substituted a-SiO_2 materials under high pressures ($\sim$60 GPa Materials in Extreme Dynamic Environments [MEDE]) relevant to ballistic events where reversible and irreversible density changes and structural transformations have been observed. If successful, such models will enable ab initio prediction of a-SiO_2 compressibility, kinetics, and "glass" phase transformations that will be used to develop equations of state for a-SiO_2 materials, and thus form a direct link to the continuum scale.

3. Develop a fully validated multiscale finite element computational model and code incorporating the effects of reversible and irreversible densification, inelastic deformation, and overlain by a spatiotemporally evolving population of growing defects, which coalesce and lead to ultimate fracture and fragmentation. It is envisioned that at some time in the not too distant future, fully concurrent multiscale computational finite element codes will be used by analysts on a regular basis for optimal material design.

The remainder of the report is organized as follows. General program objectives are outlined in section 2, and the approach for modeling the multiscale behavior of glass appears in section 3. Experimental work on various glasses is described in section 4, which also includes an overview of ballistic experiments and fragmentation studies conducted at the Ernst-Mach Institute; section 4 describes nanoindentation tests which are useful for computational validation of the MD (section 5) and peridynamics (section 7) modeling efforts. A shock Hugoniot for fused silica is determined using force-matching techniques and described in section 5. First principles quantum mechanical methods are used to model densification and bulk modulus variation with pressure in section 6. Since inelastic deformation and a polyamorphic transformation occurs simultaneously in fused silica, a model is developed to account for this coupled behavior in section 8 and compared to plate impact experiments. A short-term conceptual project to determine an effective experimental and theoretical approach to model and characterize the role of glassy materials in resisting ballistic impact was conducted by Professor Richard Lehman, Rutgers University, in section 9. Section 10 summarizes the conclusions of this progress report.

2. Program Objectives

The long-term research goal of the program is to develop a concurrent multiscale computational finite element code for optimizing or enhancing the performance of various glasses against SCJs; the initial work focuses on pure fused-silica (a-SiO_2) and chemically varied a-SiO_2 materials. As such, this objective falls squarely within the purview of the Weapons and Materials Research Directorate (WMRD), since multiscale models are constitutive models (specific to a particular material) wherein time-evolving microstructural changes, such as microcrack growth, are fully coupled to the macroscale, a phenomenon that cannot be modeled or accounted for using classical homogenization methods. A more immediate research objective is to understand why certain chemically substituted a-SiO_2 materials exhibit enhanced performance in the defeat of SCJ and other ballistic threats.

Our program objectives are threefold:

1. Develop MD process models for a series of chemically substituted a-SiO_2 materials for the prediction of glass elastic properties. This glass plays an important role in many technological applications and its structure has been inferred from neutron-diffraction, nuclear magnetic resonance, and small-angle x-ray scattering (SAXS) analysis to reveal a three-dimensional network consisting of tetrahedrally coordinated silicon (Si) whose structure is constant throughout the glass and defines its short-range order (SRO). Long-range disorder in the structure is manifested by a seemingly random variation in the Si-O-Si bond angle in adjacent tetrahedra. Despite the intense study of a-SiO_2 glass over the last several decades, much controversy still exists on the best method to model (i.e., via density functional theory, MD, Monte Carlo methods, or master equation techniques) this archetypal material for prediction of elastic properties, diffusivity, surface interactions, bond angle distribution, polyamorphism, and melt solidification. Current models that appear in the literature are often not fully validated and progress towards this goal will be made when model predictions of elastic constants for a series of chemically substituted a-SiO_2 glasses agree with experimentally determined constants.

2. Extend the MD models to study densification of the chemically substituted a-SiO_2 materials under high pressures. Since long-range order in glass is non-existent, variations in the SRO, and intermediate range order (IRO) must be responsible for the enhanced performance observed in ballistic tests on certain a-SiO_2 glasses. If this is the case, it may be possible to

use MD models to predict macroscopic ballistic performance. Since glass is subjected to extreme pressure and temperature during an SCJ event, it will be necessary to study the relationship between compressibility, kinetics, and phase transitions during high-pressure densification of a-SiO_2 glasses as manifested by changes in coordination number, ring size, and free volume. Progress towards this goal will be made when MD-derived equations of state (EOSs) agree with those obtained experimentally via diamond anvil press and plate impact experiments.

3. Develop a fully validated multiscale finite element computational model and code that incorporates the effects of reversible and irreversible densification, and inelastic deformation, overlain with a spatiotemporally evolving population of defects that grow, coalesce, and lead to ultimate fragmentation. This objective will develop a computational framework to combine the objectives from (1) and (2), and incorporate the influence of fracture initiation, growth, coalescence, and fragmentation of surface and volume defects in glass into a comprehensive concurrent multiscale finite element model and code. Microcrack initiation, growth, and coalescence (sometimes referred to as failure waves) is a multiscale phenomenon that bridges all scales in a-SiO_2 glasses despite the apparent absence of a structural mesoscale for this class of materials (figure 2). Algorithms for the development of fully two-way coupled multiscale codes are in their infancy, and progress on this objective will be realized with successful development and implementation of a consistent scheme for coarse-graining localization phenomena such as fracture failure observed in glass.

3. Planned Approach

The planned approach consists of three components, which are outlined in figure 3:

1. *Validate the MD models for a series of chemically substituted a-SiO_2 materials for the prediction of glass elastic properties.* Although there is no effort within WMRD to predict a-SiO_2 elastic properties, a hierarchical multiscale modeling effort is currently underway within WMRD, which is focused on the study of polycrystalline ($\sim$200 μm grain size) $AlON$ and validation of quantum and MD predictions of anisotropic elastic constants using diamond anvil cell (DAC) and focused-ion-beam (FIB)/scanning electron microscopy (SEM) compression tests on oriented $AlON$ single crystals (*14*). We plan to use MD methods (with possible MD coarse-graining) to simulate glass process modeling during melt solidification by quenching a high-density, high temperature, and pressure (with possible polyamorphic phases)

melt for a series of chemically substituted a-SiO_2 materials. Next, the resulting room-temperature, chemically modified structures will be reversibly deformed to predict the elastic properties that will be validated with experimentally determined elastic properties.

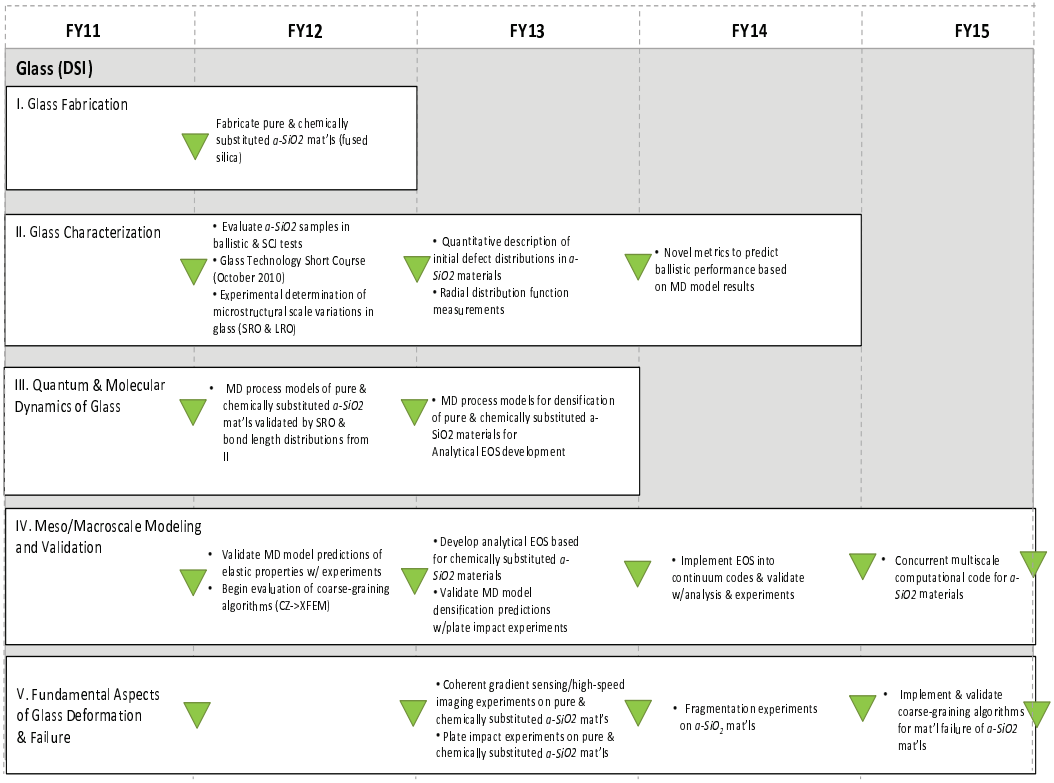

Figure 3. Five-year roadmap consistent with the WMRD brittle materials program.

2. *Validate the MD models for densification of chemically substituted a-SiO_2 materials under high pressures.* Although there is currently no effort within WMRD to predict the EOS of chemically substituted a-SiO_2 materials, MD methods have been used to predict high-pressure densification in these materials. MD simulations of pure a-SiO_2 materials reveal a Hugoniot elastic limit (HEL) of about 10 GPa, and an anomalous maximum in compressibility at around 3 GPa. Experiments where samples have been compressed to pressures lower than 10 GPa are indistinguishable from the original material, whereas above 10 GPa, materials can sustain an irreversible density increase from 10–20% higher than the starting material,

although there is controversy as to whether the mechanism is due to irreversible coordination defects or permanent ring size modification. In contrast to the behavior of a-SiO_2, crystalline quartz (α-SiO_2), undergoes very well-known high pressure polymorphic phase transitions into a Coesite phase and a Stishovite phase (figure 4), which involve changes in coordination of the Si cation from four to six O atoms. A combination of diamond anvil press and plate impact experiments will be conducted on a series of chemically substituted a-SiO_2 materials and compared with MD densification simulations in glass in order to understand the influence of glass modifiers on changes in the shock response of these materials. EOSs for a subset of promising chemically substituted materials will be developed and implemented into a continuum code to determine if any of the chemically substituted materials exhibit enhanced ballistic performance.

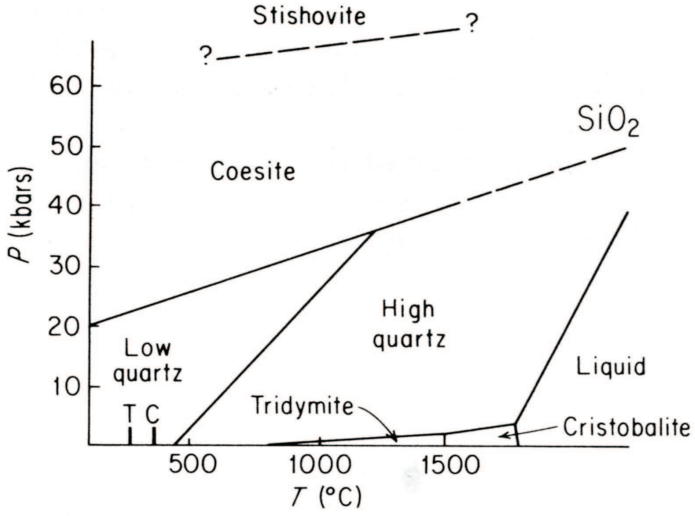

Figure 4. Crystal structures of quartz, after Frye (*2*).

3. *Develop a fully validated multiscale finite element computational model and code that incorporates the effects of reversible and irreversible densification, and inelastic deformation, overlain with an spatiotemporally varying population of defects which grow, coalesce, and lead to ultimate material fragmentation.* The ultimate research objective is to develop a physics-based multiscale computational finite element code for studying densification, and dynamic fracture in non-crystalline ceramics (see figure 2). Atomistic behavior will be linked to macroscopic elastic properties and densification behavior through development of an EOS from first principles as outlined in components (1) and (2) above. At this stage, what remains

to be accomplished, is to successfully link, in a concurrent fashion, multiscale failure phenomena in a-SiO_2 materials by incorporating the important role that pre-existing surface and volume defects have on the microcrack growth, coalescence, and fragmentation in this class of materials. Over the past five years, the first author has also been directly involved in development of a parallel, concurrent multiscale code for heterogeneous viscoelastic composites (*15*) under the auspices of a U.S. Army Research Laboratory (ARL)/University of Nebraska cooperative agreement, which will be leveraged and used as the framework for the development of a concurrent multiscale model of a-SiO_2 materials.

The chief challenge for brittle materials is to correctly account for the growth kinetics of microcracks in a multiscale computational environment. The propagation of free internal boundaries at lower scales will be "coarse-grained" to higher scales, where global fracture failure and fragmentation is observed. As such, coarse-graining algorithms will need to be validated through continuum-scale experiments on a-SiO_2 materials that measure dynamic crack propagation speeds, mixed-mode failure, and crack bifurcation phenomena using coherent gradient sensing and high-speed imaging techniques; ARL possesses capabilities for conducting such dynamic fracture experiments in a-SiO_2 materials through the recent establishment of a coherent gradient sensing/imaging facility funded by the ongoing multiscale modeling effort of $AlON$. Models and validation of the initiation and propagation of discrete fractures in a-SiO_2 materials should transition naturally into models of fragmentation and comminution for behind-armor-debris applications. Fragmentation experiments have classically been conducted using dynamically expanding ring experiments for defining fragment size versus strain rate and will be used to validate computational models of fragmentation. The development of consistent coarse-graining algorithms for fracture in materials, which is associated with failure and loss of material stability, is largely unexplored and is the primary high-risk goal of this section.

4. Experimental Work and Background

4.1 Background

4.1.1 Compositions

Silicate-based ceramic glasses are based on chemical substitutions into a SiO_4 tetrahedral-based polymeric-like structure; fused silica is an amorphous (non-crystalline) form of pure SiO_2. Table 1 lists the compositions and properties of typical glasses.

Table 1. Glass compositions in $\%$ and selected properties.

Glass	SiO_2	Al_2O_3	CaO	B_2O_3	Na_2O	K_2O	$\rho(g/cm^3)$	E (GPa)	ν
Borofloat	80.5	2.5	0.02	12.7	3.55	.64	2.23	62.3	.207
Starphire	73.2	1.44	10.27	-	14.72	.01	2.51	72.3	.23
Fused Silica	100	-	-	-	-	-	2.2	73.0	.17

4.1.2 Structural Characteristics of Ceramic Glasses

Simplistically, the predominant macro-characteristics (micron and larger) can be a variety of defects including inclusions, bubbles, large pores, and residual compressive or tensile stress. The notion of an array of crystalline grains separated by grain boundaries (a microstructure) does not exist in glass. Rather, there is a complete lack of long-range order, but short- and intermediate-range order at the nano-structural scale:

- Short-range order: Mostly atom to atom bond lengths, less than 0.5 nm and bond angles; characterized by radial distribution functions (RDFs) and SAXS.

- Intermediate-range order: In silica-based glasses, this is the polymerization of the silica atomic tetrahedra (one Si atom surrounded by four oxygen atoms) into various size ring structures of joined tetrahedra, which can consist of 4, 5, 6, 7, 8, or so ring groups of tetrahedra. Substitution of other cations (Na, K, Mg, Ca, etc.) and B into silica-based glasses can have profound effects on the intermediate-range order. It is also important to note that B bonds to three oxygen atoms in flat triangles.

- Free-volume: In crystalline materials, using the theoretical density, it is straightforward to calculate the atomically unoccupied free space. In glasses, this unoccupied atomic space is

referred to as "free volume," but because of an unknown periodic structure it is extremely difficult to quantify in glasses. The free volume plays a critical role in glass densification under stress/pressure.

- There can be significant complex spatial variations of defects, free volume, atomic structure, and resulting properties at the nanoscale.

- It is the current wisdom of the glass community that the short- and intermediate-range order at the nanoscale in glasses can have a significant influence on some properties.

4.1.3 Effect of Stress/Pressure

Deformation and failure in ceramic glasses begins with reversible to irreversible densification and/or critical cracks nucleating at defects:

- High pressure can have significant effect on coordination of Si changing from typical fourfold to sixfold coordination of oxygen around Si - (quartz-like to coesite-like to stishovite-like structures, as for crystalline quartz shown in 4).

- The degree of polymerization or distribution of the ring structures can also change as a function of pressure.

- The common consensus is that the ring distribution is the primary control of some properties; however, at very high pressures, the change from four to sixfold Si coordination will significantly influence properties as well.

- Some properties of fused silica (pure SiO_2 glass) are anomalous, e.g., a negative change in shear modulus as a function of pressure. Bando et al. (*3*) show that the radius of curvature of a crack in glass (figure 5) can be about 1.5 nm, suggesting that the intermediate-range order can significantly influence crack propagation.

Fig. 4. Crack geometry of thin silica glass film at (A) low magnification and (B) high magnification, showing crack tip.

Figure 5. The radius of curvature of a crack in glass after Bando (*3*).

4.1.4 Plasticity in Glass

Ito (*4*) has presented fairly simple methods of determining the brittleness (figure 6) or, conversely, the plasticity of glasses, which he uses to suggest that the brittleness is dependent of IRO or the distribution of ring structures seen in figure 7. Table 2 lists values for the brittleness parameters.

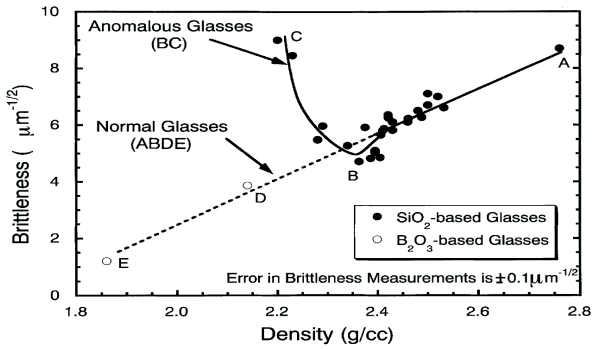

Figure 6. Brittleness vs. density for glasses in the SiO_2 and B_2O_3-based glasses, after Ito (*4*).

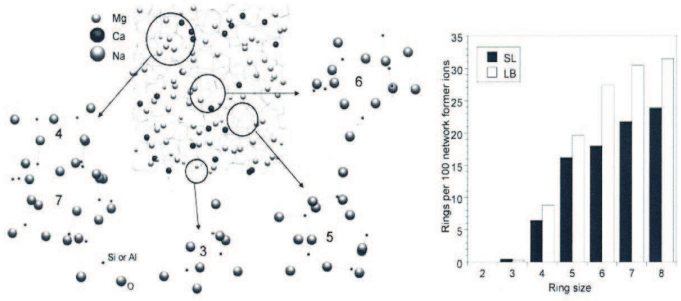

(a) (b)

Figure 7. (a) Structure of soda lime glass by MD simulation where the number shown is the ring size and (b) Number of network rings in soda lime (SL) and less brittle (LB) glasses; LB glass are more polymerized than SL glass after Ito (*4*).

Table 2. Brittleness parameters.

Glass	Brittleness Parameter ($\mu m^{-1/2}$)
Fused Silica	~10
B_2O_3 Based glass	~1
Soda Lime	~5 - 7

The brittleness, therefore, seems to be dependent on the deformation and fracture behavior, which depends on flow and densification before crack initiation and on the bond strength of the network and seems to decrease with a decrease in density—a free volume effect. This is addressed by Ito (*4*) in the same paper.

Conclusions from this work are as follows:

- Both glasses are commercial soda-lime (SL) based glasses: $(Na, K)_2O - (Mg, Ca)O$ - SiO_2.
- The less brittle (LB) glass appears to have a higher polymerized network than the SL glass, i.e., a significant difference in the ring structure distribution.
- IRO at the nanoscale seems to be controlling the brittleness of these glasses.

4.2 Experimental Results

The absorption/dissipation of deposited energy in an extreme impact event depends on the various deformation and failure/fracture mechanisms that are activated during the event. In addition, in a multiscale modeling and simulation "Protection Materials by Design" approach it is absolutely critical to experimentally determine the key properties at the various scales to validate the theoretical computational results. We have used various quasi-static indentation, edge-on-impact (EOI) and ballistic impact tests for this purpose.

4.2.1 Indentation

Studies on the deformation and fracture of glasses and AlON using a spherical 500-μm-diameter diamond indenter was recently carried out by Wilantewicz (*5*). Results for a SL (Starphire), boron substituted glass (Borofloat), fused silica, and AlON are illustrated in figure 8 and tables 3 and 4, there are significant differences in the deformation and fracture behavior of these materials.

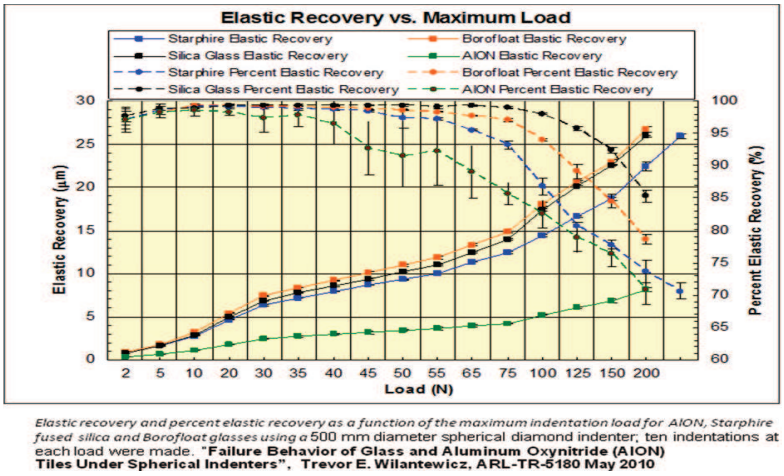

Elastic recovery and percent elastic recovery as a function of the maximum indentation load for AlON, Starphire fused silica and Borofloat glasses using a 500 mm diameter spherical diamond indenter; ten indentations at each load were made. **"Failure Behavior of Glass and Aluminum Oxynitride (AlON) Tiles Under Spherical Indenters", Trevor E. Wilantewicz, ARL-TR-5180 May 2010**

Figure 8. Elastic recovery vs. load for a variety of glasses after Wilantewicz (*5*).

Table 3. Elastic recovery in indentation tests at 200 N.

Material	% Elastic Recovery
AlON	71
Starphire	73
Borofloat	79
Fused silica	86

Table 4. Deformation and fracture loads after Wilantewicz (*5*).

Material	Onset Dimpling (N)	All Tests Dimpled (N)	Onset Ring Cracking (N)	All Tests Ring Cracked (N)	Onset Radial Cracking (N)	All Tests Radial Cracked (N)
Starphire (tin)	30	30	65	75	75	100
Starphire (air)	20	30	65	100	100	125
Borofloat (tin)	30	35	30	45	100	200
Silica Glass	75	100	20	30	65	75
AlON	35	45	45	65	40	75

It is clear that these materials behave in significantly different ways. The onset of dimpling is the result of a permanent plastic deformation. The normal expectation for these materials is that as a function of increasing indentation load the material response would proceed through an elastic regime, then through a plastic regime and finally into a cracking/fracturing regime. Table 5 summarizes the observations. Silica glass (fused silica), however, behaves in a dramatically different way, fracturing prior to a plastic mechanism.

Table 5. Onset of elastic, plastic, and fracture responses after Wilantewicz (*5*).

Material	Response
Starphire:	elastic → plastic → fracture
Borofloat:	elastic → plastic → fracture
Silica Glass:	elastic → fracture → plastic
AlON:	elastic → plastic → fracture

4.2.2 Edge-on-impact Studies of Fused Silica

The experimental arrangement is illustrated in figure 9 and a series of time resolved photographs are presented in figure 10.

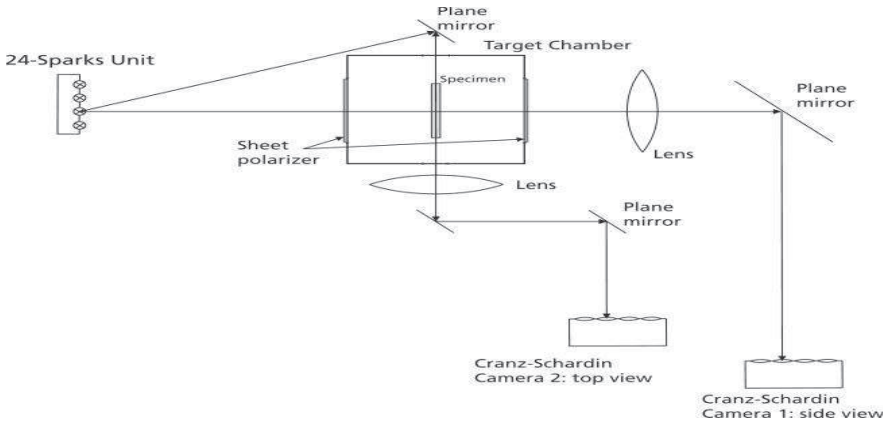

Figure 9. EOI experimental arrangement after Strassburger et al. (*6*).

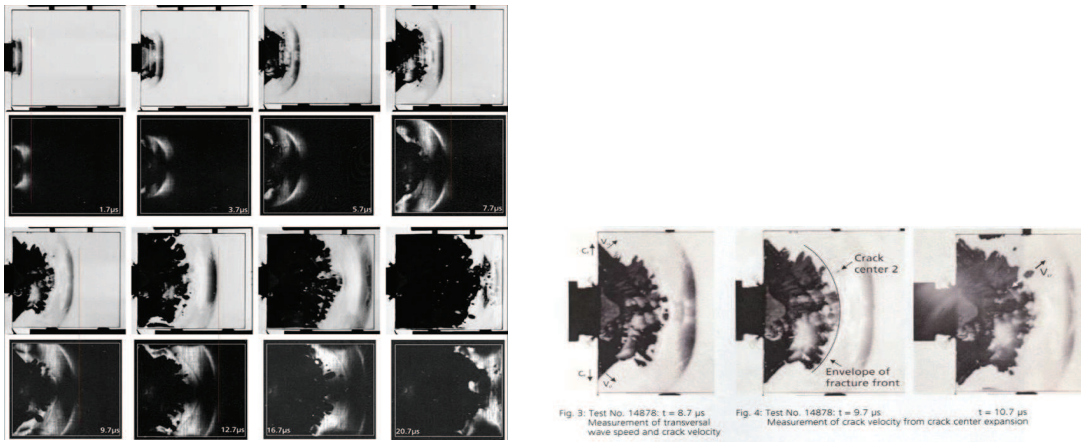

(a) (b)

Figure 10. (a) Illustration of a series of EOI tests in fused silica by a steel solid cylinder at 350 m/s at various times; first and third rows illustrate shaodwgraph photos in plane light showing damage; second and fourth rows are photos in crossed polarized light, which show the propagation of stress via a photoelastic effect, and (b) illustrates the irregular nature of the damage front due to the presence of macro-defects from the same test after Strassburger et al. (*6*).

Table 6 lists the measured velocities of the longitudinal waves, transverse waves (shear waves), and crack and damage front velocities in fused silica. Note that the longitudinal wave velocity for fused silica is 5.93 km/s and the shear wave velocity is 3.77 km/s.

Table 6. Compilation of measured wave, crack, and damage velocities in fused silica after Strassburger et al. (*6*).

Impact velocity (m/s)		150	260	350
Longitudinal wave speed (m/s)	shadowgraphs	5975	6076	5823
Longitudinal wave speed (m/s)	crossed polarizers	5814	5796	5491
Transverse wave speed (m/s)	shadowgraphs	-	3500	3670
Crack velocity (m/s)	shadowgraphs	2234	2149	2120
Damage velocity (m/s)	shadowgraphs	5641	5728	5121

4.2.3 Visualization and Analysis of Ballistic Impact Damage and Fragmentation in Various Glass Plates

In this series of experiments Borofloat, Starphire, and fused silica were tested in a standard ballistic configuration. The plates were impacted by a 7.62-mm AP round, and a solid steel cylinder inside of a box to contain all of the resulting fragments. The fragments were removed from the box with a vacuum and then sorted by sieves. Figure 11 illustrates the experimental arrangement.

Table 7 lists the details of the various tests conducted on the three glass types. Note that the dimensions of the Borofloat glass plate used in test, #17742, were significantly different than the others, which has skewed the fragmentation results at the largest sieve size 2 mm. Figure 12 illustrates a series of very-high-speed photographs as a function of time for the four tests listed in table 7.

Table 7. Test parameters with different types of glass.

EMI Test #	Type	Dimensions (mm)	Thickness (mm)	Projectile	Impact Velocity (m/s)
17742	Borofloat	149.4 x 149.7	12.94	cylinder	1089
17749	Fused silica	101.65 x 101.67	12.75	cylinder	1107
17750	Fused silica	101.62 x 101.62	12.75	7.62 AP	824
17751	Starphire	99.9 x 99.7	10.06	cylinder	1115

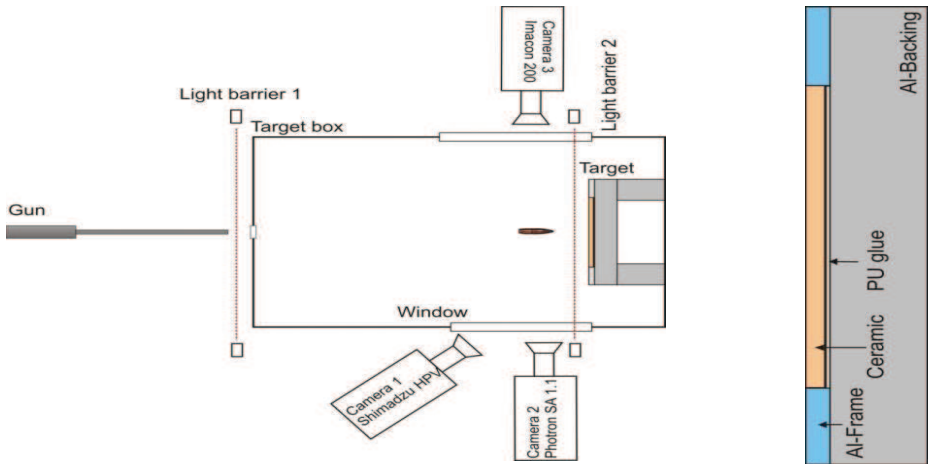

(a) (b)

Figure 11. Schematic of (a) ballistic test configuration, and (b) target after Strassburger et al. (*7*).

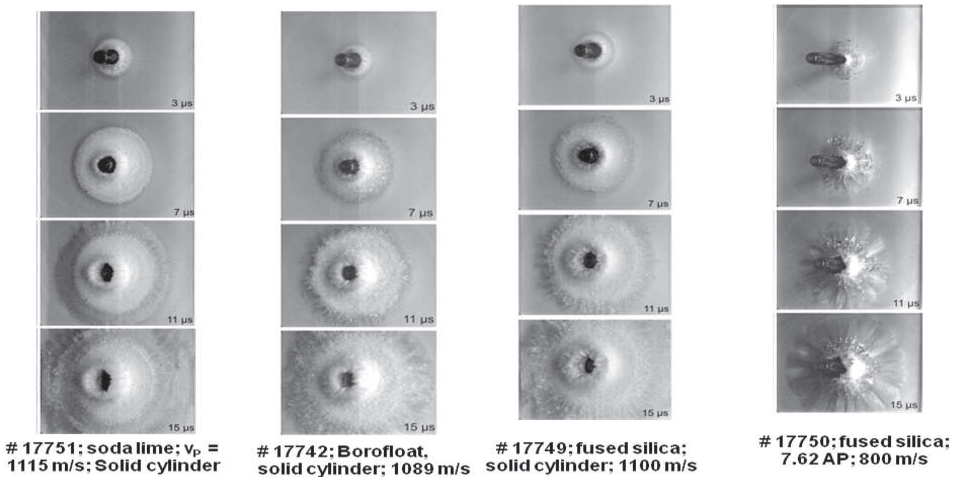

Figure 12. Selection of high-speed photographs from impact on various glasses after Strassburger et al. (*7*).

The observed propagation velocities of the damage zone under impact of the steel cylinder are all below the transverse wave velocities of the materials, as seen in table 8, which compiles the wave and fracture velocity data determined from EOI tests along with data from the actual test series. When fused silica was impacted by the 7.62-mm AP projectile, the formation of single radial cracks were observed, which propagated at an average velocity of 2394 m/s, which is in very good agreement with the crack velocity determined for fused silica from EOI tests.

Table 8. Compilation of wave and fracture velocity data after Strassburger et al. (*7*).

Glass Type	Longitudinal Wave Velocity (m/s)	Transverse Wave Velocity (m/s)	Terminal Crack Velocity (m/s)	Damage Velocity (m/s)
Starphire	5890	3570	1580	$3073^{\oplus}$
Borosilicate	5543	-	2034	$2857^{\oplus}$
Fused Silica	6021	3858	2400	$3007^{\oplus}$, $2394^{\dagger}$

$^{\oplus}$ steel cylinder, v = 1100 m/s

† AP projectile, v = 824 m/s

Figure 13 illustrates the fragmentation data of the various glasses listed in table 7. The data in the 2-mm range should be ignored as the plate size of this sample was much different than the others. The fracture and damage morphologies using the solid cylinders compared to the AP round resulted in a pronounced wave-like pattern compared to Hertzian-like radial cracking with differing radial patterns. Analysis of the fragmentation characteristics is still underway.

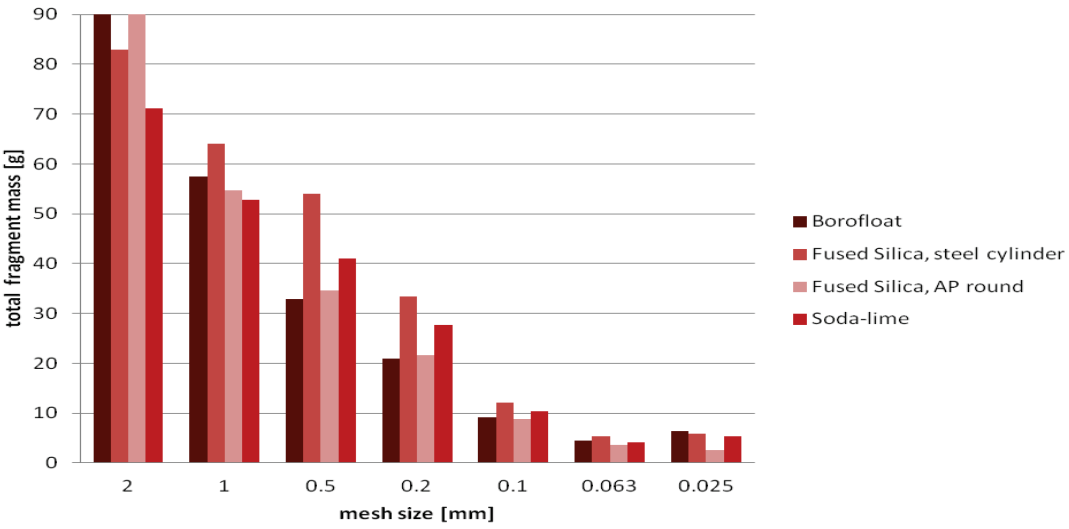

Figure 13. Fragment mass distribution from sieve analysis for tests with various glasses after Strassburger et al. (*7*).

4.2.4 Nanoindentation Studies of Fused Silica

Nanoindentation experiments were conducted at ARL on fused silica specimens using an MTS Nanoindenter XP operated in continuous stiffness measurement (CSM) mode. A spherical indenter with a radius of 3 μm was used to indent to depths approaching 2 μm at a constant strain rate of 0.05/s. The hardness values, H, were calculated from the maximum loads, P_{max}, and the contact area, A, at the maximum indentation depth where $H = \frac{P_{\max}}{A}$. The elastic modulus values were calculated using the Oliver and Pharr method (*16*) from the measured unloading stiffness, S (which is equivalent to the slope of the initial unloading curve) as follows:

$$S = \frac{2}{\sqrt{\pi}} E_{eff} \sqrt{A} \tag{1}$$

where E_{eff} is a function of the Poisson's ratio and elastic modulus for the indenter (ν_i, E_i) and material of interest (ν, E) defined as

$$\frac{1}{E_{eff}} = \frac{1-\nu^2}{E} + \frac{1-\nu_i^2}{E_i} \tag{2}$$

Following the indentation experiments, the residual indents were examined with a NanoSEM 600 SEM operated in low-vacuum mode (which is used to accommodate non-conductive specimens.)

Figure 14 shows the typical load-displacement curves for maximum displacements ranging from 500 to 2000 nm. Figure 15a plots the measured hardness as a function of indentation depth and indicates there is some indentation size effect over the range considered. The standard deviation is largest for the smallest indentation depths (500 nm). The elastic moduli decrease with increasing maximum indentation depth (figure 15b); however, the error in measurement does not follow a trend with depth. The SEM examination gives insight into the indentation size effect. We are unable to resolve a residual impression for the specimens indented to a depth limit of 500 nm, which indicates the response is mostly elastic at small depths. Figures 16–18 show SEM micrographs for specimens indented to depths of 1000, 1500, and 2000 nm, respectively. There is a noticeable residual indent in figure 16; however, there is evidence of fracture. At greater indentation depths, radial cracks (figures 17a and 18) and classic cone cracks (figure 17b) are visible. Further investigation is required, but the lower hardness and modulus values measured at greater indentation depths could result from indentation cracks. In some brittle material systems, "pop-ins" or discrete jumps in displacement during indentation are found in the load-displacement curves. However, no pop-ins are observed in this series of nanoindentation tests.

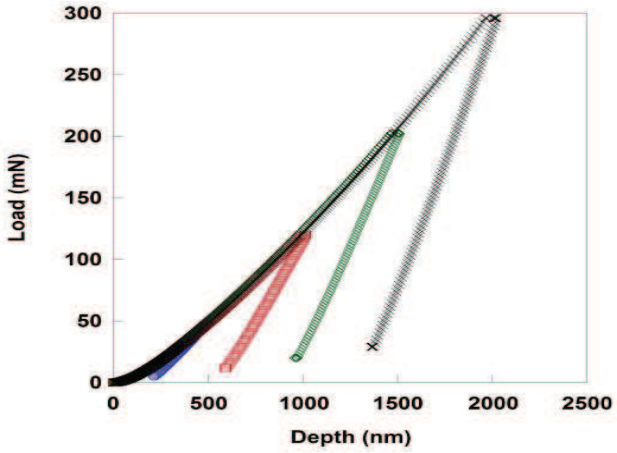

Figure 14. Load vs. displacement in fused silica.

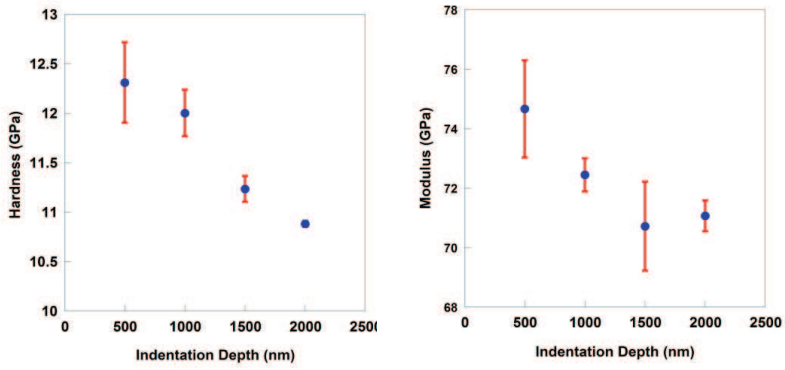

(a) (b)

Figure 15. (a) Hardness and (b) modulus variations in fused silica.

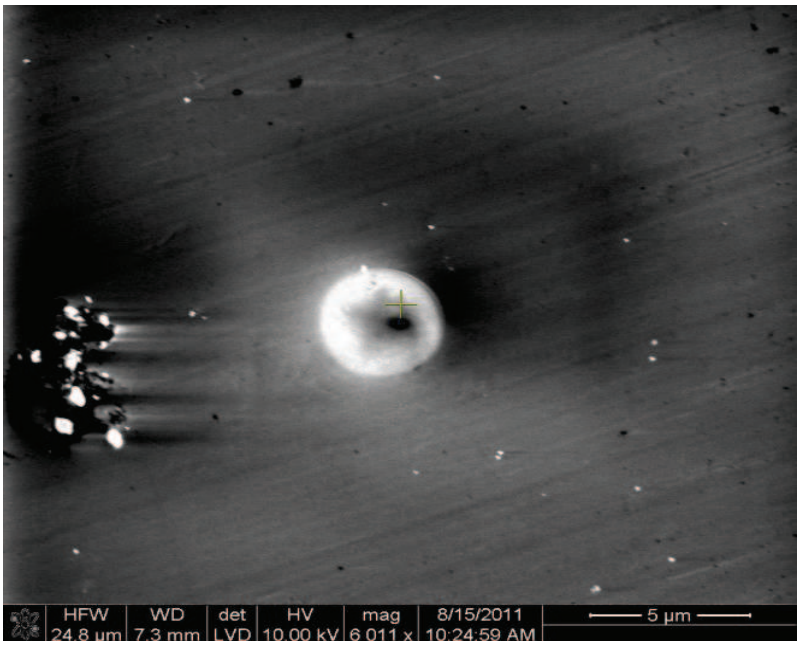

Figure 16. SEM micrographs of fused silica indented to 1000 nm.

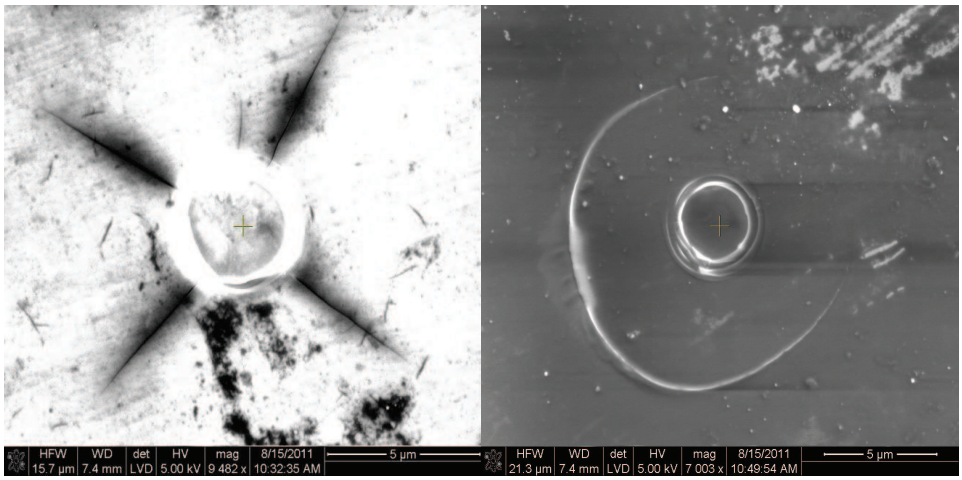

(a) (b)

Figure 17. SEM micrographs of fused silica indented to 1500 nm.

Figure 18. SEM micrographs of fused silica indented to 2000 nm.

5. Molecular Dynamics Modeling of Glass Nanoindentation

MD methods have been used to study nanoindentation for a number of material systems, i.e., metals (*17*), ceramics (*18*), glasses (*19*), and energetic materials (*20*). Length scales for MD simulations can be made comparable to those in the experiments of Nomura et al. (*19*), although the time scales and strain rates differ significantly. The advantage of MD simulations over nanoindentation experiments is the capability to provide atomistic detail of numerous properties, including stress distribution and structural information.

This section describes preliminary MD simulations of the nanoindentation of a large-scale fused silica system. All the simulations were performed using the Large-scale Atomic/Molecular Massively Parallel Simulator (LAMMPS) (*21*). The interatomic potential used in this study is a pairwise potential recently developed using force matching techniques (*11*). Force matching is a fitting approach to produce classical force fields from trajectories and forces obtained from ab initio simulations and described in Izvekov et al. (*10*). The development of such a potential was necessary due to inadequacies of existing silica potentials in describing shock properties, as shown in figure 19 and described in Gazonas et al. (*22*), which compares experimental and predicted shock Hugoniot information using existing standard classical force fields and that generated using force matching. Also, unlike the standard classical force fields, the force matched potential predicts the anomalous densification of silica at high pressures.

The amorphous phase of SiO_2 (a-SiO_2) was generated via simulated annealing. In general, there are two means of annealing a system from a melt to achieve an amorphous phase: by decreasing the temperature in discrete intervals or by continually decreasing the temperature during the course of the simulation. In both cases, the system is simulated in the constant volume-constant temperature (NVT) ensemble, with periodic boundaries in all three directions, to ensure that the final density matches the experimental value. For this study, we have chosen the former method, and followed the annealing schedule described in Pedone et al. (*8*). The temperature of the system is decreased from 5000 K in 500-K increments, resulting in a cooling rate of 10 K/ps.

The system in this study consists of 1,160,952 atoms (386,984 a-SiO_2 molecules), in a simulation cell with initial dimensions of 29.9 x 29.9 x 17.8 nm. After annealing the system, indentation is performed by a spherical indenter with a radius of 9 nm, as seen in figure 20. The indenter interacts with atoms in the simulation cell via a force of magnitude

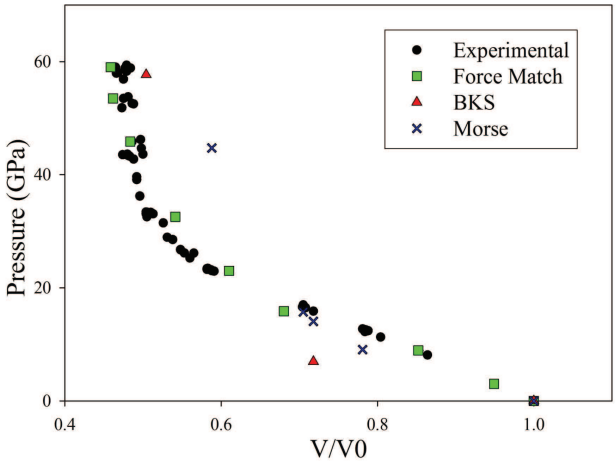

Figure 19. Comparison of experimental and simulated Hugoniot curves for fused silica (a-SiO_2): experiment (●), Morse (*8*) potential (×), BKS (*9*) potential (▲), and ARL Force Matching method (*10, 11*) (■) .

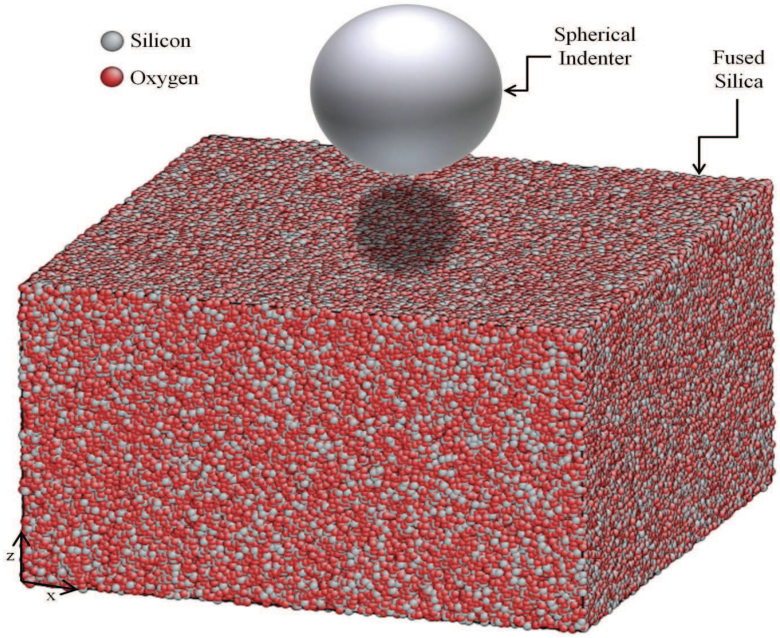

Figure 20. The initial configuration of the fused silica system, with a representation of the spherical indenter.

$$F = -K(r - R)^2 \tag{3}$$

where K is a force constant (given a value of 100.0 eV/Å^3 our current simulations), R is the radius of the indenter, and r is the distance from the atom to the center of the indenter. The indenter is initially centered at x = y = 13.45 nm, and z = 26.8 nm, so that the edge of the indenter is near the surface of the fused silica system. The indenter is given a velocity of 0.05 Å/ps (5 m/s) in the negative z direction. The system can be unloaded at any time by reversing the velocity of the indenter. In order to ensure that the system remains stationary during indentation, approximately 33,000 atoms (those with z < 0.5 nm) are held fixed. Periodic boundary conditions are implemented in the x- and y-directions, while the indented surface remains free. The simulation is performed in the microcanonical ensemble (NVE), with a timestep of 2.0 fs. The simulation is run for 800,000 timesteps, for a total simulation time of 1.6 ns. Figure 21 shows a cross section of the atomic configuration at four different times, and the corresponding force versus distance curve is shown in figure 22. The force in figure 22 is the z-component of the force on the indenter. The force increases with distance as expected, although the curve begins to plateau near the end of the simulation. This is most likely due to the proximity of the indenter to the frozen atoms at the bottom of the simulation cell. No pileup around the indenter is observed, and no cracking occurs during loading. The system is unloaded from an earlier point in the simulation, when the indenter depth is approximately 4.0 nm, to avoid artificial effects from the frozen atoms. The complete loading and unloading curve is shown in figure 23a. The cross sections of the corresponding atomic configurations at the maximum load and after complete unloading are shown in figures 23b and 23c, respectively. From these images, we see that some elastic recovery has taken place. The hardness is estimated as the maximum load divided by the projected area of the indent and is determined to be 8.1 GPa. This is slightly less than the experimental value of 10 GPa determined by Miyake et al. (*23*); however, these simulations must be repeated on larger systems to ensure that the size of the sample is not adversely affecting the hardness results. Additionally, future simulations will explore the effects of strain rate and indenter size, and will be directly compared to recent experimental results described in subsection 4.2.4 in an effort to determine the atomistic mechanisms driving the mechanical response of the system during nanoindentation.

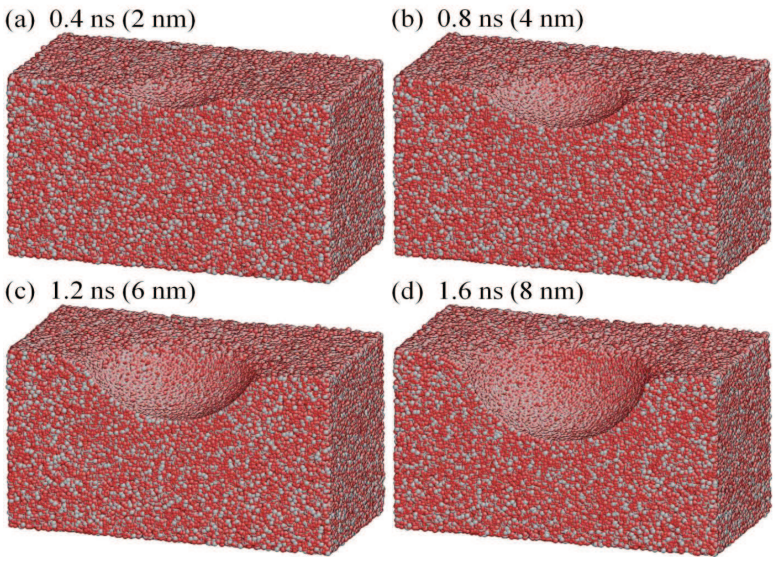

Figure 21. Cross section of the atomic configuration at the indicated times. The distances in parentheses indicate the indentation depth.

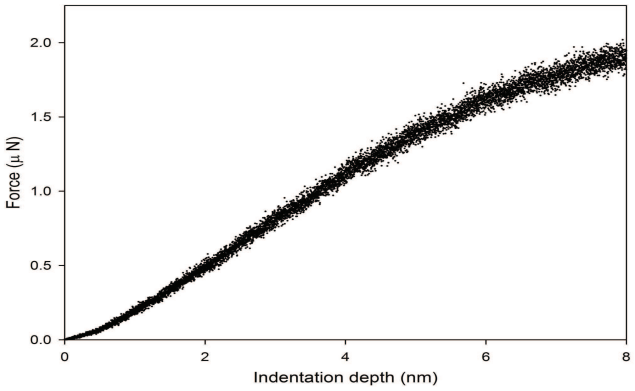

Figure 22. The z-component of the force on the indenter plotted against the indentation depth corresponding to the system in figure 21.

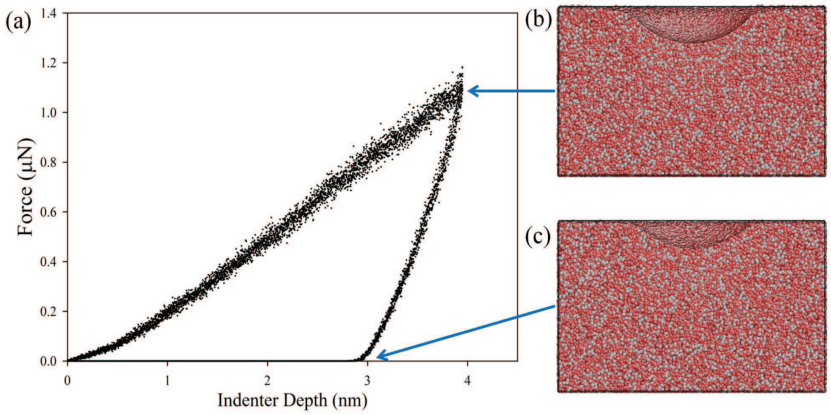

Figure 23. (a) Force vs. indenter depth for a complete loading and unloading cycle. Atomic configuration (b) at the point of maximum loading, and (c) after complete unloading.

6. Quantum Mechanics Modeling of Densification and Bulk Modulus of Silica Versus Pressure

A detailed understanding of the densification process and structural changes in amorphous solids under pressure is appealing for both experimental and simulation work. One of the interesting questions is about the nature of the structural transformation between low and high density amorphous phases. To model the structure under pressure from first principles, we used models with different density, number of atoms, and different ring statistics. We used two different methods to generate the random connected networks (1) a Monte-Carlo bond switching model (72 and 114 atom models) and (2) MD simulated annealing of melted silica. The ring statistics could be described by plots of ring size distribution seen in figure 24. The faster the quenching of the melt is, the wider is the distribution of the ring sizes. Here is an example of slow quenching with ring distributions from 4 to 8 member rings, which corresponds to the quartz-like structure of the 114 atom model. Two other models with 72 and 192 atoms have wider distribution of the ring sizes from 3 to 12 member rings; for reference, quartz has only 6 member rings. Three to four member rings have a low concentration, but play an important role because they correspond to the most reactive sites. The angles between the $Si-O-Si$ atom, and the $O-Si-O$ atom distributions also convey important information about structural changes under certain pressure (figure 25).

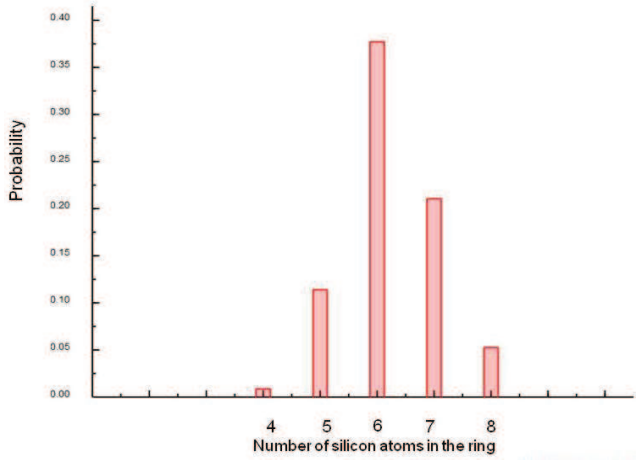

Figure 24. Ring distribution for 114 atom model.

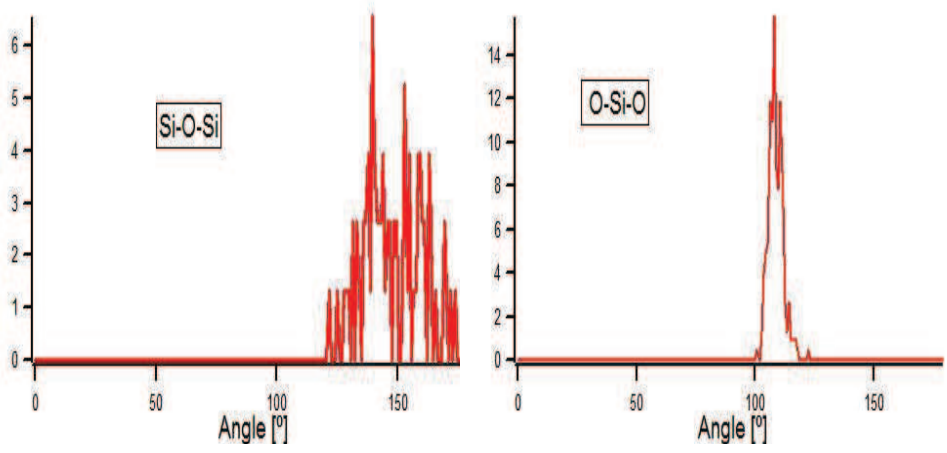

Figure 25. Two types of angle distribution in the 114 atom model.

By relaxing the internal coordinates under compressive or tensile pressures at normal conditions, we found that the $Si - O - Si$ angle ranges between 130° and 180°, while the tetrahedral units are preserved. This result is in good agreement with previous theoretical and experimental results of Mauri et al. (*24*). Clear signs of structural transformations in silica under the pressure may be seen from the calculated mass density (figure 26). We did the calculations of density after optimizing the shape and volume of the unit cell without projections in real space. The analysis used the Projector Augmented Wave (PAW) method implemented in the Vienna ab initio simulation package (VASP) code described in Kresse and Hafner (*25*).

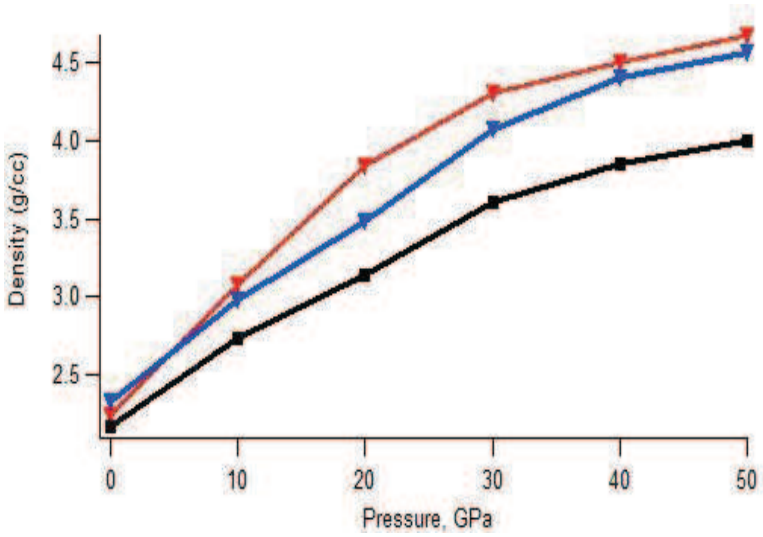

Figure 26. Density of fused silica as a function of pressure for 72 atom (▼), 114 atom (▼), and 192 atom (■)models.

In all three models, one may see two slopes of density, which might be related with different types of structural changes. One occurs up to 20–30 GPa, and another region is from 30–50 GPa. Some signatures of the two phases may be seen from the x-ray absorption experiments of Sato and Funamori (*12*) (figure 27).

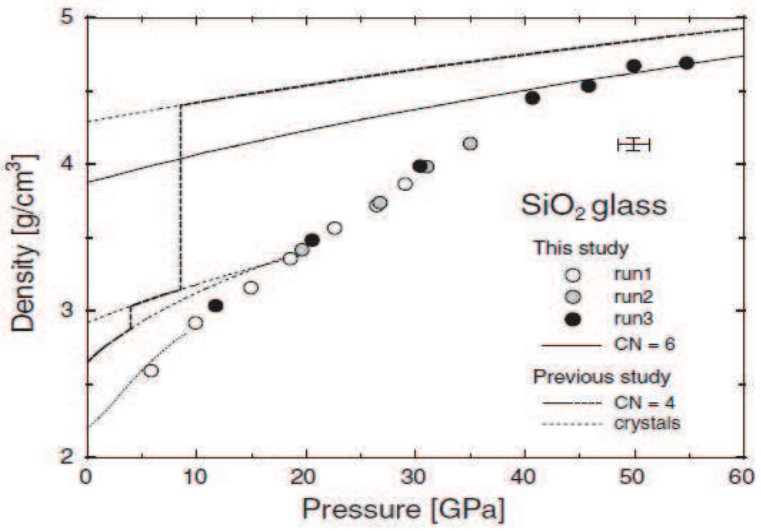

Figure 27. Experimental density of fused silica after Sato and Funamori (*12*).

To understand what is so special with these two stages of structural transformation in silica, we did angle distribution analysis under pressures similar to that depicted in figure 25. It turned out that in the first region there is not much change in $O - Si - O$ distribution, but discernible changes in $Si - O - Si$ distribution indicating that up to 20–30 GPa there is a squeezing of space between tetrahedra and not much distortion of tetrahedrons. Each O atom has two nearest neighbors; each Si atom has four nearest neighbors. While after 30-GPa silica becomes very dense, and both $Si - O - Si$ and $O - Si - O$ angles change, revealing transformation in both the tetrahedra and the space between them. At 40–50 GPa severe distortion of the tetrahedrons resulted in formation of sixfold-coordinated Si atoms (figure 28). The DFT observation of the sixfold-coordinated atoms confirms the assumption suggested in Sato and Funamori (*12*).

A manifestation of the two phases of silica densification might exhibit the unusual behavior of the elastic constants, particularly the bulk modulus. We calculated the bulk modulus from the stress-strain relationship for 114-atom model. The bulk modulus of fused silica generally increases with pressure, but unusual behavior of the pressure dependence up to 20 GPa may be related to the densification of the space between the tetrahedra (figure 29). A second region after 20 GPa with significant increase of bulk modulus corresponds to the densely packed tetrahedra.

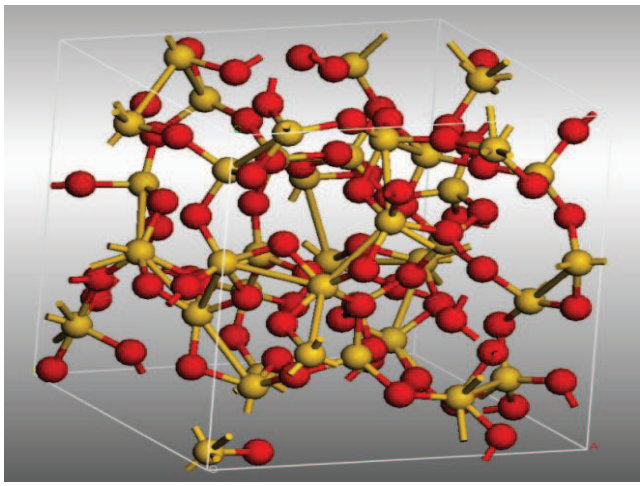

Figure 28. Fused silica structure under 50-GPa with sixfold-coordinated Si atoms.

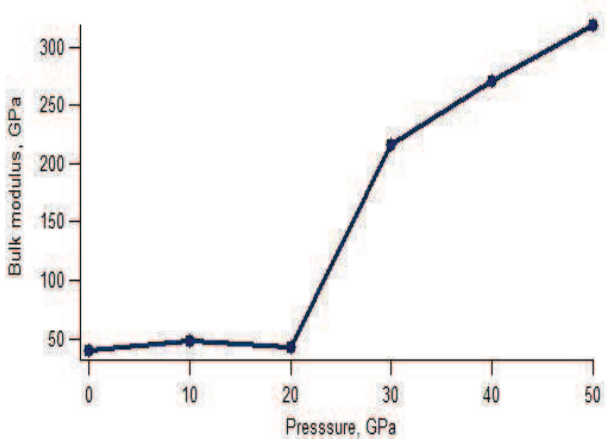

Figure 29. Bulk modulus of fused silica as a function of pressure.

6.1 Force Matching Pair Potentials for Borosilicate Glasses

To generate pair potentials for borosilicate glasses we used the force matching method developed by Izvekov and Rice (*11*). The method is based on DFT calculations of trajectories in Born-Oppenheimer approximation at 5000 K. The pair potentials for $S - B$ and $B - O$ generated using the method are shown in the figure 30.

Pair $Si - Si$, $Si - O$, and $O - O$ potentials are similar to those used for pure silica MD calculations. The numerical pair potentials include to a certain extent many body interactions since they were generated based on force matching of DFT calculations.

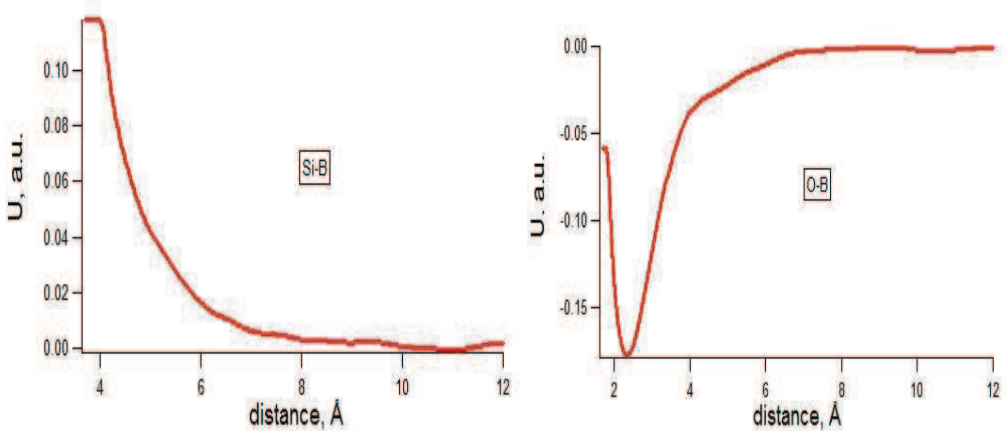

(a) (b)

Figure 30. Pair potentials for (a) $Si - B$ and (b) $O - B$.

7. A Perfectly Matched Layer for Peridynamics in Two Dimensions

In this section, we develop a peridynamic method for modeling nanoindentation experiments in fused silica and other chemically substituted glasses. Originally introduced in Silling (*26*), peridynamics is a non-local formulation of elastodynamics, which can more easily incorporate discontinuities such as cracks and damage. Derivatives of field variables in the classical continuum model are replaced by integrals over a small neighborhood of microelastic kernels, which replaces the standard constitutive relation. In its discretized form, an elastic solid is treated as a collection of particles or nodes, each connected to its neighbors by breakable bonds.

Bond breakage can be defined to occur when a bond is stretched past some predetermined limit. The end result is a method capable of predicting crack growth in brittle elastic materials (*27–32*). The original formulation was limited to materials with a fixed Poisson's ratio of 0.25; however, state-based peridynamics was introduced allowing for more flexible constitutive relations (*33*). As will become clear later, state-based peridynamics allows for an auxiliary field formulation, which is necessary for the implementation of a perfectly matched layer (PML). While most peridynamics work has focused on simulating problems with free or fixed boundary conditions, there are applications in which the simulation of an infinite medium may be useful, such as crack propagation in a halfspace or nanoindentation problems. Absorbing boundary conditions are one way of simulating an infinite medium as any impinging waves are suppressed so they do not reflect back into the simulation. A PML is such an absorbing boundary, and was originally introduced for electromagnetic simulations (*34, 35*). PMLs differ from traditional absorbing boundary conditions in that they are an absorbing layer with a finite width, placed between the computation region of interest and the truncation of the grid or mesh. They can also be thought of as an anisotropic absorbing material, which is why the flexibility of a state-based peridynamics is necessary. A PML was applied to one-dimensional (1-D) peridynamics (*36*), which used the results of Du et al. (*37*) to formulate an auxiliary field equation. This approach required a matrix representation of the auxiliary field, which may be memory prohibitive in higher dimensions.

7.1 Two-dimensional (2-D), State-based Peridynamics

The continuum equation of motion in an elastic solid can be stated as

$$\rho \frac{\partial^2}{\partial t^2}\mathbf{u} = \nabla \cdot \overline{\boldsymbol{\sigma}} + \mathbf{b} = \nabla \cdot (\overline{\mathbf{c}} : \overline{\boldsymbol{\epsilon}}) + \mathbf{b}, \tag{4}$$

where $\rho(\mathbf{x})$ is the density, $\mathbf{u}(\mathbf{x}, t)$ is the displacement, $\overline{\boldsymbol{\sigma}}(\mathbf{x}, t)$ is the stress tensor, $\overline{\boldsymbol{\epsilon}}(\mathbf{x}, t)$ is the strain tensor, $\overline{\mathbf{c}}$ is the stiffness matrix for plane strain, defined by Young's modulus E, Poisson's ratio ν, or Lamé parameters λ and μ, and $\mathbf{b}(\mathbf{x})$ is a body force (*38*). (Throughout, boldface type denotes a vector and a boldface variable with an overbar denotes a tensor.) Equation 4 is a local formulation because the divergence of the stress (and gradient of the displacement implied in its definition) represents a local operation on a variable. In other words, the action of $\nabla \cdot \overline{\boldsymbol{\sigma}}$ only depends on $\overline{\boldsymbol{\sigma}}$ at a single spatial point. In problems involving discontinuities, such as cracks, the divergence at such discontinuities is not well defined, leading to numerical implementation problems. Peridynamics proposes replacing $\nabla \cdot \overline{\boldsymbol{\sigma}}$ with a nonlocal operation that nonetheless also represents a force. Here, we use the state-based peridynamics (*33*), rather than the original bond-based version (*26*). A PML application requires an auxiliary field formulation, as it is essentially an anisotropic absorbing material, if a non-physical one. Consequently, a state-based

peridynamic formulation is necessary to implement the required constitutive relations in the absorber. The state-based peridynamics uses a family of bonds to determine a given force rather than a single bond independently. This more general approach allows for inelastic behavior and more general elastic behavior, and is governed by

$$\rho\frac{\partial^2}{\partial t^2}\mathbf{u} = \int_{\mathcal{H}_\mathbf{x}} \left(\overline{\mathbf{T}}[\mathbf{x},t]\langle\mathbf{x}'-\mathbf{x}\rangle - \overline{\mathbf{T}}[\mathbf{x}',t]\langle\mathbf{x}-\mathbf{x}'\rangle\right) dV' + \mathbf{b}, \tag{5}$$

where $\mathcal{H}_\mathbf{x}$ is the horizon region, defined as a circle centered at $\mathbf{x}$ with radius δ, $\overline{\mathbf{T}}[\mathbf{x},t]\langle\mathbf{x}'-\mathbf{x}\rangle$ is a peridynamic vector state, with parameters in the square brackets indicating variables that act as arguments to any functions that define the vector state and variables in the angle brackets acting as arguments to the vector state itself. In the state-based formulation, the deformation gradient, given by

$$\overline{\mathbf{F}} = \bar{\mathbf{I}} + \mathbf{u}\nabla, \tag{6}$$

can be approximated as a vector state as

$$\overline{\mathbf{F}}[\mathbf{x},t] = \left[\int_{\mathcal{H}_\mathbf{x}} C(|\boldsymbol{\xi}|)\left(\mathbf{Y}[\mathbf{x},t]\langle\boldsymbol{\xi}\rangle \otimes \boldsymbol{\xi}\right) dV_{\mathbf{x}'}\right]\overline{\mathbf{K}}^{-1}, \tag{7}$$

where $C(|\boldsymbol{\xi}|) = \exp(-|\boldsymbol{\xi}|^2/\delta^2)$ is a shape function, taken as a Gaussian distribution here and with the horizon $\mathcal{H}_\mathbf{x}$ extended so that the shape function decays to an arbitrary, small value, taken here as 10^{-6}, $\overline{\mathbf{K}}$ is a shape tensor given by

$$\overline{\mathbf{K}}[\mathbf{x},t] = \int_{\mathcal{H}_\mathbf{x}} C(|\boldsymbol{\xi}|)\left(\boldsymbol{\xi}\otimes\boldsymbol{\xi}\right) dV_{\mathbf{x}'}, \overline{\mathbf{K}}^{-1} = \begin{bmatrix} k_{xx}^{-1} & k_{xy}^{-1} \\ k_{yx}^{-1} & k_{yy}^{-1} \end{bmatrix}, \tag{8}$$

and $\mathbf{Y}$ is a deformation vector state given by

$$\mathbf{Y}[\mathbf{x},t]\langle\boldsymbol{\xi}\rangle = \boldsymbol{\eta} + \boldsymbol{\xi}, \tag{9}$$

with $\boldsymbol{\eta} = \mathbf{u}[\mathbf{x}',t] - \mathbf{u}[\mathbf{x},t]$ and $\boldsymbol{\xi} = \mathbf{x}' - \mathbf{x}$ (*39*).

The deformation gradient can now be substituted into Hooke's law and strain-displacement relations, giving a stress term $\overline{\boldsymbol{\sigma}}$ in terms of $\mathbf{u}$ in plane strain

$$\rho\frac{\partial^2}{\partial t^2}\mathbf{u} = \nabla\cdot\overline{\boldsymbol{\sigma}} = \nabla\cdot\left(\overline{\mathbf{c}} : \overline{\boldsymbol{\epsilon}}\right), \tag{10}$$

where

$$\overline{\boldsymbol{\epsilon}}[\mathbf{x},t] = \frac{1}{2}\left(\nabla\mathbf{u} + \mathbf{u}\nabla\right) \approx \frac{1}{2}\left(\overline{\mathbf{F}}[\mathbf{x},t] + \overline{\mathbf{F}}[\mathbf{x},t]^{\mathrm{T}} - 2\bar{\mathbf{I}}\right). \tag{11}$$

Ultimately, the peridynamic vector state $\mathbf{T}$ for plane strain elasticity is given by

$$\overline{\mathbf{T}}[\mathbf{x}, t]\langle \boldsymbol{\xi} \rangle = C(|\boldsymbol{\xi}|)\overline{\boldsymbol{\sigma}}[\mathbf{x}, t]\overline{\mathbf{K}}^{-1}\boldsymbol{\xi}. \tag{12}$$

7.2 Auxiliary Field Formulation and PML Application

The first step in formulating a PML is to construct an analytic continuation to the complex plane, such as $\hat{x} = x + ig(x)$, where $g(x)$ is a given function describing the deformation (*40*). This mapping has the effect of transforming traveling waves of the form e^{ikx}, where $k = \omega/c$ is the wave number, into evanescent waves of the form $e^{ikx}e^{-kg(x)}$, thus attenuating such waves in the PML region. Applying a PML involves substituting for spatial derivatives using

$$\frac{\partial}{\partial x} \rightarrow \frac{1}{1 + i\frac{\phi(x)}{\omega}}\frac{\partial}{\partial x}. \tag{13}$$

The function $\phi(x)$ defines the extent of the PML region, i.e., when $\phi(x) = 0$ the original wave equation is obtained, and when $\phi(x) > 0$, traveling waves decay exponentially. Typically, $\phi(x)$ transitions from 0 to a constant value using a smooth function to prevent numerical reflections at the boundary between the absorbing and computational regions. Before applying a PML directly to the peridynamic equation, equation 4 will be treated so that the PML application to peridynamics will be clear. It is convenient to convert equation 4 to the Laplace domain, assuming e^{-st} time dependence, and express the wave equation as two coupled first order partial differential equations, the first in $\tilde{\mathbf{u}}$ and the second in $s\tilde{\overline{\boldsymbol{\psi}}} = \tilde{\overline{\boldsymbol{\sigma}}}$

$$\begin{aligned} \rho s\tilde{\mathbf{u}} &= \nabla \cdot \tilde{\overline{\boldsymbol{\psi}}} \\ s\tilde{\overline{\boldsymbol{\psi}}} &= \overline{\mathbf{c}} : \tilde{\overline{\boldsymbol{\epsilon}}}, \end{aligned} \tag{14}$$

where the Laplace transform of a variable is indicated by $\mathcal{L}\{f\} = \tilde{f}$. Expanding equation 14 into components gives five coupled equations

$$
\begin{aligned}
\rho s\tilde{u}_x &= \frac{\partial}{\partial x}\tilde{\psi}_x + \frac{\partial}{\partial y}\tilde{\psi}_\tau \\
\rho s\tilde{u}_y &= \frac{\partial}{\partial x}\tilde{\psi}_\tau + \frac{\partial}{\partial y}\tilde{\psi}_y \\
s\tilde{\psi}_x &= (\lambda + 2\mu)\frac{\partial}{\partial x}\tilde{u}_x + \lambda\frac{\partial}{\partial y}\tilde{u}_y \\
s\tilde{\psi}_y &= \lambda\frac{\partial}{\partial x}\tilde{u}_x + (\lambda + 2\mu)\frac{\partial}{\partial y}\tilde{u}_y \\
s\tilde{\psi}_\tau &= \mu\left(\frac{\partial}{\partial y}\tilde{u}_x + \frac{\partial}{\partial x}\tilde{u}_y\right).
\end{aligned}
\tag{15}
$$

We can expand the state-based formulation into components and match terms to equation 15. Following this approach yields a viable method for performing PML substitutions. First, the state-based peridynamic equations listed above in equations 5–12 can be written explicitly as

$$
\begin{aligned}
\rho s\tilde{u}_x[\mathbf{x},s] &= \int_{\mathcal{H}_\mathbf{x}} C(|\boldsymbol{\xi}|)\left[\left(\tilde{\psi}_x[\mathbf{x},s]k_{xx}^{-1} + \tilde{\psi}_\tau[\mathbf{x},s]k_{yx}^{-1}\right)\xi_x + \left(\tilde{\psi}_x[\mathbf{x}',s]k_{xx}^{-1} + \tilde{\psi}_\tau[\mathbf{x}',s]k_{yx}^{-1}\right)\xi_x\right]dV_{\mathbf{x}'} \\
&\quad + \int_{\mathcal{H}_\mathbf{x}} C(|\boldsymbol{\xi}|)\left[\left(\tilde{\psi}_x[\mathbf{x},s]k_{xy}^{-1} + \tilde{\psi}_\tau[\mathbf{x},s]k_{yy}^{-1}\right)\xi_y + \left(\tilde{\psi}_x[\mathbf{x}',s]k_{xy}^{-1} + \tilde{\psi}_\tau[\mathbf{x}',s]k_{yy}^{-1}\right)\xi_y\right]dV_{\mathbf{x}'}, \\
\rho s\tilde{u}_y[\mathbf{x},s] &= \int_{\mathcal{H}_\mathbf{x}} C(|\boldsymbol{\xi}|)\left[\left(\tilde{\psi}_\tau[\mathbf{x},s]k_{xx}^{-1} + \tilde{\psi}_y[\mathbf{x},s]k_{yx}^{-1}\right)\xi_x + \left(\tilde{\psi}_\tau[\mathbf{x}',s]k_{xx}^{-1} + \tilde{\psi}_y[\mathbf{x},s]k_{yx}^{-1}\right)\xi_x\right]dV_{\mathbf{x}'} \\
&\quad + \int_{\mathcal{H}_\mathbf{x}} C(|\boldsymbol{\xi}|)\left[\left(\tilde{\psi}_\tau[\mathbf{x},s]k_{xy}^{-1} + \tilde{\psi}_y[\mathbf{x},s]k_{yy}^{-1}\right)\xi_y + \left(\tilde{\psi}_\tau[\mathbf{x}',s]k_{xy}^{-1} + \tilde{\psi}_y[\mathbf{x},s]k_{yy}^{-1}\right)\xi_y\right]dV_{\mathbf{x}'}, \\
s\tilde{\psi}_x[\mathbf{x},s] &= (\lambda + 2\mu)\left[\int_{\mathcal{H}_\mathbf{x}} C(|\boldsymbol{\xi}|)\left(\tilde{Y}_x[\mathbf{x},s]\xi_x k_{xx}^{-1} + \tilde{Y}_x[\mathbf{x},s]\xi_y k_{yx}^{-1}\right)dV_{\mathbf{x}'} - 1\right] \\
&\quad + \lambda\left[\int_{\mathcal{H}_\mathbf{x}} C(|\boldsymbol{\xi}|)\left(\tilde{Y}_y[\mathbf{x},s]\xi_x k_{xy}^{-1} + \tilde{Y}_y[\mathbf{x},s]\xi_y k_{yy}^{-1}\right)dV_{\mathbf{x}'} - 1\right], \\
s\tilde{\psi}_y[\mathbf{x},s] &= \lambda\left[\int_{\mathcal{H}_\mathbf{x}} C(|\boldsymbol{\xi}|)\left(\tilde{Y}_x[\mathbf{x},s]\xi_x k_{xx}^{-1} + \tilde{Y}_x[\mathbf{x},s]\xi_y k_{yx}^{-1}\right)dV_{\mathbf{x}'} - 1\right] \\
&\quad + (\lambda + 2\mu)\left[\int_{\mathcal{H}_\mathbf{x}} C(|\boldsymbol{\xi}|)\left(\tilde{Y}_y[\mathbf{x},s]\xi_x k_{xy}^{-1} + \tilde{Y}_y[\mathbf{x},s]\xi_y k_{yy}^{-1}\right)dV_{\mathbf{x}'} - 1\right], \\
s\tilde{\psi}_\tau[\mathbf{x},s] &= \mu\int_{\mathcal{H}_\mathbf{x}} C(|\boldsymbol{\xi}|)\left(\tilde{Y}_x[\mathbf{x},s]\xi_x k_{xy}^{-1} + \tilde{Y}_x[\mathbf{x},s]\xi_y k_{yy}^{-1}\right)dV_{\mathbf{x}'} \\
&\quad + \mu\int_{\mathcal{H}_\mathbf{x}} C(|\boldsymbol{\xi}|)\left(\tilde{Y}_y[\mathbf{x},s]\xi_x k_{xx}^{-1} + \tilde{Y}_y[\mathbf{x},s]\xi_y k_{yx}^{-1}\right)dV_{\mathbf{x}'},
\end{aligned}
\tag{16}
$$

etc. Though no derivatives appear in equations 16, the correspondence of each term to those in

equation 15 is apparent and the PML substitutions can be made. For example, the first equation in 16 can be rewritten as

$$\begin{aligned}\rho\left(s+\phi_x\right)\left(s+\phi_y\right)\tilde{u}_x = &\left(s+\phi_y\right)\int_{\mathcal{H}_{\mathbf{x}}} C(|\boldsymbol{\xi}|)\left(\tilde{\psi}_x[\mathbf{x},s]k_{xx}^{-1}+\tilde{\psi}_{xy}[\mathbf{x},s]k_{yx}^{-1}\right)\xi_x dV_{\mathbf{x}'}\\ &+\left(s+\phi_y\right)\int_{\mathcal{H}_{\mathbf{x}}} C(|\boldsymbol{\xi}|)\left(\tilde{\psi}_x[\mathbf{x}',s]k_{xx}^{-1}+\tilde{\psi}_{xy}[\mathbf{x}',s]k_{yx}^{-1}\right)\xi_x dV_{\mathbf{x}'}\\ &+\left(s+\phi_x\right)\int_{\mathcal{H}_{\mathbf{x}}} C(|\boldsymbol{\xi}|)\left(\tilde{\psi}_x[\mathbf{x},s]k_{xy}^{-1}+\tilde{\psi}_{\tau}[\mathbf{x},s]k_{yy}^{-1}\right)\xi_y dV_{\mathbf{x}'}\\ &+\left(s+\phi_x\right)\int_{\mathcal{H}_{\mathbf{x}}} C(|\boldsymbol{\xi}|)\left(\tilde{\psi}_x[\mathbf{x}',s]k_{xy}^{-1}+\tilde{\psi}_{\tau}[\mathbf{x}',s]k_{yy}^{-1}\right)\xi_y dV_{\mathbf{x}'},\end{aligned} \tag{17}$$

with the remaining equations following similarly. The final step involves simply converting back to the time domain and implementing a forward Euler discretization scheme in time, and the standard one-point integration method (*32*) in space.

7.3 Results

The previous method was numerically implemented using a forward Euler method for the temporal discretization, and standard one-point integration with point-matching in space. In the following example, a 1 m-by-1 m region was used with a Gaussian pulse initial condition set for the x-directed displacement. For the PML, a Gaussian ramp was used as a smooth transition to a constant value, set at 50 s^{-1}, with the constant region having a width 0.1 m and the ramp a width of 0.2 m. Young's modulus was set to 1 Pa, Poisson's ratio was set to 0.25, and the density was set to 1 g/m^2. The simulation was run for 8 s. Figure 31 shows the total strain energy, summed over the entire region, as a function of time. As can be seen, the PML absorbing boundary layer absorbs impinging waves and reduces the total energy by five orders of magnitude. Figure 32 shows a waterfall plot of the x-directed displacement along the $y = 0.5$ m line. This plot also shows the decay of the displacement as it enters the PML region.

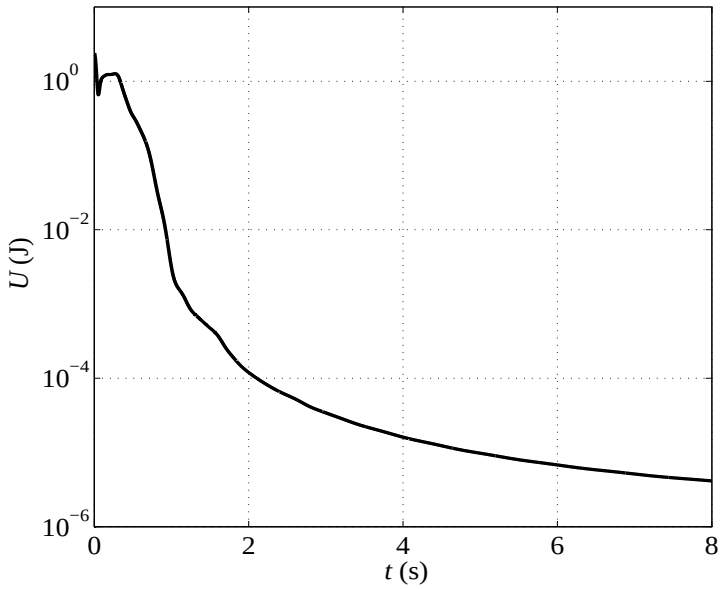

Figure 31. Total strain energy in a simulation terminated by a PML.

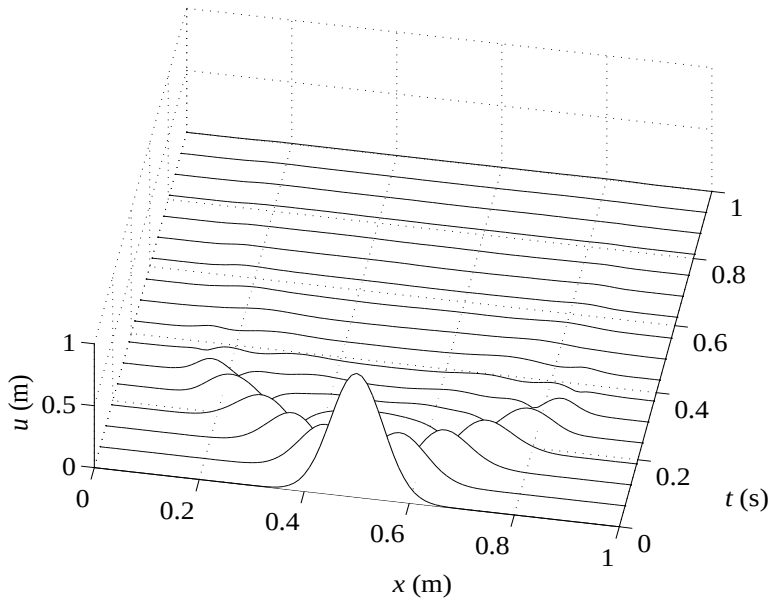

Figure 32. x-directed displacement at $y = 0.5$ m, terminated by a PML.

8. Continuum Equation-of-state Model Development

Established processes to develop constitutive models for use in large scale analysis and design simulations are heavily influenced by the vast body of work on metals. Typically, a model is split into an EOS, relating pressure, density, energy and temperature, and a strength model, which relates the deviatoric part of the stress tensor to the time history of the strain rate, temperature, and state variables. This is the context of the glass EOS in Gazonas et al. (*22*) where a polyamorphic model was used, in conjunction with high and low pressure EOS models, to represent the permanent volume change in glass at high pressures (in excess of 10 GPa).

The model assumptions are evaluated by comparison of simulation results with velocity profiles obtained from gas gun experiments by Alexander et al. (*13*). The experimental results are shown for three different impact velocities in figure 33a. The initial velocity ramp from 0 to 0.2 km/s results from the decreasing modulus with pressure, which is not captured by the current model. At velocities of approximately 0.6 km/s there is a kink associated with the polyamorphic transformation. The high velocity curve (208 m/s impact velocity) rises abruptly after the transformation point, and caps at a velocity consistent with the initial velocity and shock impedance of the flyer. The transformation is nearly over driven at this high velocity, in that there is very little shift between the two vertical sections of the curve. The lower curve (137 m/s) shows a gradual rise associated with the kinetics of the transformation. It reaches the peak velocity by the end of the plot. The profile from the intermediate velocity experiment retains some curvature due to the transformation kinetics, but the steady velocity is attained quickly.

Results from using the initial model, with separate elastic-plastic and polyamorphic transformations, in gas gun simulations yields velocity profiles displaying a three-wave structure (figure 33b rather than the two waves seen in the experiments. The model kinetics were assumed to be fast in these simulations to accentuate the steps. The first rise in the profile ends with the HEL associated with the elastic-plastic transition. The second rise ends with the volume change from the polyamorphic transformation, and the third rise terminates with the maximum particle velocity. From this comparison, it is evident that the elastic-plastic and polyamorphic transformations must occur concurrently, or an extra step will appear in the velocity profile. Physically, this implies that the atoms move to accommodate shear strain as they are rearranging to accommodate the volume change.

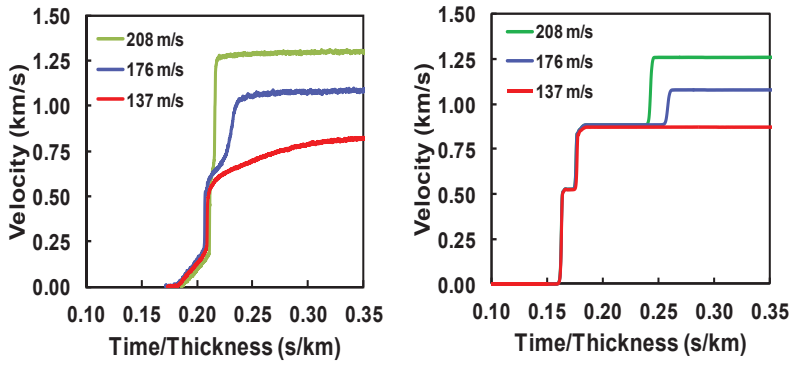

Figure 33. Velocity profiles from: (a) gas gun experiments on borosilicate glass from Alexander et al. (*13*) and (b) simulations using independent functions for the elastic-plastic transition and the polyamorphic transformation.

The modeling goal is to couple inelastic deviatoric deformation and volume change. There is no experimental data to guide the functional form for the coupling, so a simple quadratic flow potential model is assumed:

$$\phi = 0 = \sqrt{\alpha\sigma_e^2 + p^2} - \bar{p}(\lambda). \tag{18}$$

Here, σ_e is the effective stress, p is the pressure, and $\bar{p}$ is a function of the volume fraction of the low pressure polyamorph, λ. α is a parameter regulating the relative influence of the deviatoric stress compared to the pressure.

Following concepts used in metal plasticity, the direction of inelastic flow is assumed to be normal to the flow potential:

$$\mathbf{d}_{inelas} = \Lambda \frac{\partial \phi}{\partial \boldsymbol{\sigma}}, \tag{19}$$

where $\mathbf{d}_{inelas}$ is the inelastic part of the rate of deformation tensor, $\mathbf{d}$, which is decomposed, additively, into elastic and inelastic parts $\mathbf{d} = \mathbf{d}_{elas} + \mathbf{d}_{inelas}$. The elastic part is also a function of the stress tensor through the elastic moduli. Together these provide a coupled set of equations for Λ in equation 19, which is determined by an iterative procedure.

The volume fraction of the low density polyamorph is assumed to evolve through a kinetic relation

$$\dot{\lambda} = \beta(\lambda - \lambda_\infty)^3 e^{(\nu \frac{T - T_{ref}}{T_{ref}})} \tag{20}$$

where β and ν are parameters and λ_∞ represents the equilibrium fraction of the low density polyamorph. The equilibrium phase fraction

$$\lambda_\infty = \left(\frac{\bar{p}_f - \bar{p}}{\bar{p}_f - \bar{p}_t} \right)^2 \tag{21}$$

is a function of the applied loading, $\bar{p}$, the threshold pressure at which the transformation begins, $\bar{p}_t$, and the pressure at which the glass is fully transformed to the high density polyamorph, $\bar{p}_f$.

These equations were implemented into a finite element code and the gas gun simulations run. Figure 34a shows the results with the kinetic parameter set high (β = 100) to give the equilibrium response. From these calculations it is evident that a two-wave structure is produced, indicating that the inelastic deformation and polyamorph transformation are occurring simultaneously. Figure 34b shows the results with a kinetic parameter (β = 3) set to reproduce the basic features observed in the experimental data plotted in figure 33a.

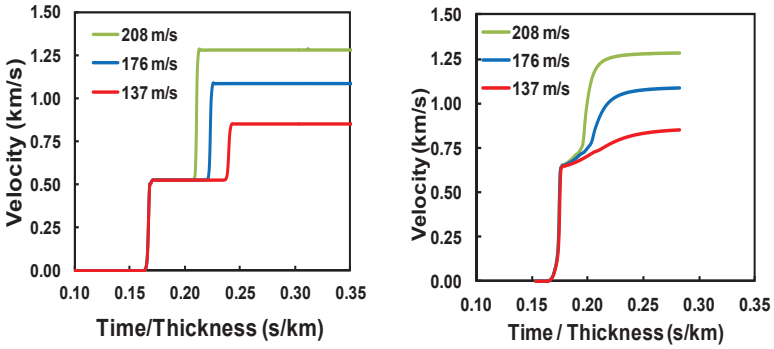

(a) (b)

Figure 34. Gas gun simulation results for a model with concurrent elastic-plastic transition and polyamorphic transformation and with (a) a high kinetic parameter for rapid transformation and (b) the kinetic parameter adjusted to resemble experiments.

The simulation results demonstrate some general model features necessary to reproduce experimental observations from high-pressure gas gun experiments. The model must couple the deviatoric stress and the pressure for the polyamorphic transformation, and a kinetic model is necessary to introduce time-dependent rises in the response. Other features may also be necessary, but these two have a major impact and provide a well defined starting point for model improvement. The particular functional relations assumed for this model are conjecture guided by experience in modeling metals. Hence, appropriate data are needed to guide model development. While it will be possible to tune a kinetic parameter based on data from current experimental methods, existing experimental techniques will provide little information on the functional form for the kinetic relation or the flow function dependence on deviatoric stress and pressure. The alternative, and the approach pursued in the program, is to determine the functional relationships and parameters through multiscale modeling approaches.

9. A Short-term Conceptual Project

A short-term conceptual project to determine an effective experimental and theoretical approach to model and characterize the role of glassy materials in resisting ballistic impact was conducted by Richard Lehman, Professor and Chair of the Department of Materials Science and Engineering, Rutgers University, Piscataway, NJ. A short synopsis of the report was delivered to ARL on November 17, 2011 and appears below.

A number of features of the glassy state are thought to participate in the ballistic response of glass including:

- Structural relaxation/viscoelasticity/strain energy equivalence theory (SEET)
- Short- and longer-range atomic structural characteristics
- Free volume (compaction, bulking)
- Cation and anion coordination
- Bond energies
- Other nanoscale order characteristics that are difficult to determine experimentally for silicate glasses.

A number of expert personnel were contacted with the following panel discussion outcomes:

- Structural relaxation: The ability of glass to convert to a liquid with little structural adjustment compared to crystalline materials may enable glass to respond more favorably to shaped charge

assault within the microsecond time periods of the impact. Viscoelastic issues will be addressed.

- Modeling: Structural models based on statistical thermodynamics, ring structures, molecular dynamics, and, anisotropic finite element methods (FEMs) will be considered. Experimental pair distribution functions based on x-ray data will be discussed.

- Molecular defects: Glass is rich in molecular defects such as oxygen hole centers, E, bridging oxygen, non-bridging oxygen, and various ring defect structure. These defects may play an important role in the shaped charge behavior.

- Heterogeneous structure: Most glasses are not the uniform isotropic material at the mesoscale that many scientists assume. Phase separation, cation clustering, and small-scale density fluctuations (as evidenced by various types of optical scattering) may be important in allowing glass to accommodate high strain rates.

- Free-volume: Glasses contain a large amount of free volume compared to their crystalline counterparts.

Summary and conclusions of the study include the following:

- MDs can be expanded into the mesoscale region:
  - Large atom arrays (>10^9) and non-cubic shapes, e.g., high aspect ratio cylinders.
  - Use surrogates to boost scale.
  - Time scale (microseconds) cannot be collapsed and is a major limit on modeling time.

- FEMs can be down-scaled to the mesoscale size region:
  - Requires specialized nonlinear methods.
  - Structural elements modeled as nonlinear elements.
  - Xi Chen at Columbia Univ. has relevant experience.

- Medium-ranged structural data obtained with scanning tunneling electron microscopy (STEM):
  - Initial material characterization.
  - Input to modeling effort.
  - Aid in interpretation of stress wave work.
- Stress wave characterization:
  - Coherent acoustic phonon spectroscopy is a promising dynamic approach.
  - The time scale is very short.
  - Experiments can be adjusted to span a range of experimental time periods.

10. Conclusions

This second-year progress report on multiscale modeling of noncrystalline ceramics (glass) has focused on establishing the framework for development of a multiscale computational methodology for optimizing or enhancing the performance of fused silica materials not yet synthesized. A more immediate research objective is to understand why certain chemically substituted fused silica materials exhibit enhanced performance in the defeat of SCJs and other ballistic threats. Conclusions consistent with the milestones shown in the five-year roadmap shown in figure 3 are as follows:

1. Fused silica and various chemically substituted silica specimens have been delivered to ARL under the auspices of an ongoing cooperative agreement; these specimens have been ballistically tested, and will serve to validate future computational models of fused silica.

2. The structural characteristics of silica glasses include SRO consisting of atom to atom bond lengths that are less than 0.5 nm and bond angles characterized by RDFs and SAXS measurements. IRO in silica-based glasses consists of the polymerization of the silica atomic tetrahedra (one Si atom surrounded by four O atoms into ring structures of joined tetrahedra of a variety of sizes ranging from 4 to 8 groups of tetrahedra). Chemical substitution of Na, K, Mg, Ca and other atoms can have a profound effect on IRO and ballistic performance. Initial free volume and its variation with pressure control densification behavior, but this is difficult to measure or quantify, especially at elevated pressure. A glass brittleness parameter discussed by Ito (*4*) appears dependent on the deformation and fracture behavior which depends on flow and densification before crack initiation and on the bond strength of the network and seems to decrease with a decrease in density.

3. A series of experiments on Borofloat, Starphire, and fused silica were conducted at Ernst-Mach Institute, which showed that fracture and fragmentation (figure 13) of these glasses have profoundly different macroscopic response (figure 12) and fracture kinetics (table 8) useful for computational model validation. Solid cylinder impact onto fused silica targets results in a greater mass of finer fragments than the AP round, whereas the AP round results in a larger mass of greater than 2-mm-size fragments (figure 13).

4. A series of nanoindentation experiments (indenter radius = 3 μm) into fused silica were conducted at ARL, which showed that both hardness and modulus decreased with increasing indentation depth. Also, both radial and cone cracks were observed in indents, which

exceeded 1500 nm (figures 17 and 18). The nanoindentation experiments will be used to validate molecular dynamics and peridynamics models of fused silica and other chemically substituted glasses.

5. Preliminary MD simulations of nanoindentation (indenter radius = 9 nm) into fused silica were conducted using LAMMPS (*21*) using a pairwise interatomic potential developed using novel force-matching techniques described in Izvekov and Rice (*11*) and Izvekov et al. (*10*). A shock Hugoniot for fused silica to 60 GPa was also calculated using a force-matched potential, which is in excellent agreement with experimental values (figure 19).

6. First principles quantum mechanical methods using VASP (*25*) are used to model densification and bulk modulus variations with pressure in fused silica. Ring size distributions (figure 24) and angle distributions for $Si-O-Si$ and $O-Si-O$ (figure 25) are calculated, and future work will consider the pressure variation of these distributions and whether they can be validated with experimental measurements conducted on fused silica under extreme pressure using diamond anvil cells. Force-matched potentials were also determined for a borosilicate glass system (figure 30).

7. A 2-D peridynamic model was developed to model nanoindentation and dynamic crack propagation in fused silica as an extension of the recent 1-D model of Wildman and Gazonas (*36*). A PML was added to permit infinite computational domains that are encountered in solution to certain boundary value problems.

8. Since inelastic deformation and a polyamorphic transformation apparently occurs simultaneously in some glasses, a model was developed to account for this coupled behavior, which captures the kinetics of the polyamorphic transformation that occur in plate impact experiments on borosilicate (compare for example the plate impact experiments of Alexander et al. (*13*) in figure 33a with simulation results in figure 34b.

INTENTIONALLY LEFT BLANK.

11. References

1. Moran, B.; Glenn, L. A.; Kusubov, A. Jet penetration in glass. *J. Phys. IV* **1991**, *1 (C3)*, 147–154.

2. Frye, K. *Modern Mineralogy;* Prentice-Hall, Inc.: Englewood Cliffs, NJ, 1974.

3. Bando, Y.; Ito, S.; Tomozawa, M. Direct observation of crack tip geometry of SiO_2 glass by high-resolution electron microscopy. *J. Am. Ceram. Soc.* **1984**, *67* (3), C36-C37.

4. Ito, S. Structural study on mechanical behavior of glass. *J. Ceram. Soc. Jpn.* **2004**, *112* (1309), 477–485.

5. Wilantewicz, T. E. *Failure behavior of glass and aluminum oxynitride (AlON) tiles under spherical indenters*; ARL-TR-5180; U.S. Army Research Laboratory: Aberdeen Proving Ground, MD, 2010.

6. Strassburger, E.; Patel, P.; McCauley, J.; Templeton, D. W. High-speed photographic study of wave and fracture propagation in fused silica. In *Proceedings of the* 22^{nd} *International Symposium on Ballistics*; Vancouver, BC, 2005.

7. Strassburger, E.; Bauer, S.; Hunzinger, M. Analysis of the fragmentation of AlON and bi-modal grain sized spinel. In *Interim Report, Report E 39/11, Contract No. W911NF-10-2-0100*; 2011.

8. Pedone, A.; Malavasi, G.; Menziani, M. C.; Cormack, A. N.; Segre, U. A new self-consistent empirical interatomic potential model for oxides, silicates, and silica-based glasses. *J. Phys. Chem. B* **2006**, *110* (24), 11780–11795.

9. van Beest, B. W. H.; Kramer, G. J.; van Santen, R. A. Force-fields for silicas and aluminophosphates based on ab initio calculations. *Phys. Rev. Lett.* **1990**, *64* (16), 1955–1958.

10. Izvekov, S.; Parrinello, M.; Burnham, C. J.; Voth, G. A. Effective force fields for condensed phase systems from ab initio molecular dynamics simulation: A new method for force-matching. *J. Chem. Phys.* **2004**, *120* (23), 10896–10913.

11. Izvekov, S.; Rice, B. M. Mechanism of densification in silica glass under pressure as revealed by bottom-up pairwise effective interaction model. *J. Chem. Phys.* **2011**, (submitted).

12. Sato, T.; Funamori, N. Sixfold-coordinated amorphous polymorph of SiO_2 under high pressure. *Phys. Rev. Lett.* **2008**, *101* (25).

13. Alexander, C. S.; Chhabildas, L. C.; Reinhart, W. D.; Templeton, D. W. Changes to the shock response of fused quartz due to glass modification. *Int. J. Impact Eng.* **2008**, *35*, 1376–1385.

14. Gazonas, G. A.; McCauley, J. W.; Batyrev, I. G.; Casem, D.; Clayton, J. D.; Dandekar, D. P.; Kraft, R.; Love, B. M.; Rice, B. M.; Schuster, B. E.; Weingarten, N. S. Multiscale modeling of armor ceramics: Focus on AlON. In *Proceedings of the 27th Army Science Conference*; Orlando, FL, 2010.

15. Souza, F. V.; Allen, D. H. Multiscale modeling of impact on heterogeneous viscoelastic solids containing evolving microcracks. *Int. J. Numer. Meth. Eng.* **2010**, *82* (4), 464–504.

16. Oliver, W.; Pharr, G. Measurement of hardness and elastic modulus by instrumented indentation: Advances in understanding and refinements to methodology. *J. Mater. Res.* **2004**, *19* (1), 3-20.

17. Saraev, D.; Miller, R. E. Atomistic simulation of nanoindentation into copper multilayers. *Model. Simul. Mater. Sci. Eng.* **2005**, *13* (7), 1089-1099.

18. Janakiraman, N.; Aldinger, F. Yielding, strain hardening, andccreep under nanoindentation of precursor-derived $Si-C-N$ ceramics. *J. Am. Ceram. Soc.* **2010**, *93* (3), 821-829.

19. Nomura, K.; Chen, Y.-C.; Kalia, R. K.; Nakano, A.; Vashishta, P. Defect migration and recombination in nanoindentation of silica glass. *Appl Phys. Lett.* **2011**, *99* (11).

20. Chen, Y.-C.; Nomura, K.; Kalia, R. K.; Nakano, A.; Vashishta, P. Molecular dynamics nanoindentation simulation of an energetic material. *Appl Phys. Lett.* **2008**, *93* (17).

21. Plimpton, S. J. *LAMMPS Users Manual: Large-scale Atomic/Molecular Massively Parallel Simulator;* Sandia Corporation: Sandia National Laboratories, 2003.

22. Gazonas, G. A.; McCauley, J. W.; Batyrev, I. G.; Becker, R. C.; Patel, P.; Rice, B. M.; Weingarten, N. S. *Multiscale modeling of non-crystalline ceramics (glass)*; ARL-MR-0765; U.S. Army Research Laboratory: Aberdeen Proving Ground, MD, 2011.

23. Miyake, K.; Fujisawa, S.; Korenaga, A.; Ishida, T.; Sasaki, S. The effect of pile-up and contact area on hardness test by nanoindentation. **2004**, *43* (7B), 4602-4605; 11th International Colloquium on Scanning Probe Microscopy (ICSPM 11), Haitsu, Japan, December 11-13, 2003.

24. Mauri, F.; Pasquarello, A.; Pfrommer, B.; Yoon, Y.; Louie, S. $Si-O-Si$ bond-angle distribution in vitreous silica from first-principles Si-29 NMR analysis. *Phys. Rev. B* **2000**, *62* (8), R4786-R4789.

25. Kresse, G.; Hafner, J. Norm-conserving and ultrasoft pseudopotentials for first-row and transition-elements. *J. Phys.: Condens. Mat.* **1994**, *6* (40), 8245–8257.

26. Silling, S. Reformulation of elasticity theory for discontinuities and long-range forces. *J. Mech. Phys. Solids* **2000**, *48* (1), 175–209.

27. Demmie, P. N.; Silling, S. A. An approach to modeling extreme loading of structures using peridynamics. *J. Mech. Mater. Struct.* **2007**, *2* (10), 1921–1945.

28. Gerstle, W.; Sau, N.; Silling, S. Peridynamic modeling of plain and reinforced concrete. In *18^{th} International Conference on Structural Mechanics in Reactor Technology*; Beijing, China, 2005.

29. Ha, Y. D.; Bobaru, F. Studies of dynamic crack propagation and crack branching with peridynamics. *Int. J. Fracture* **2010**, *162* (1-2), 229–244.

30. Emmrich, E.; Weckner, O. The peridynamic model in non-local elasticity theory. In *Proceedings in Applied Mathematics and Mechanics*; Vol. 6; 2006.

31. Kilic, B.; Agwai, A.; Madenci, E. Peridynamic theory for progressive damage prediction in center-cracked composite laminates. *Compos. Struct.* **2009**, *90* (2), 141–151.

32. Silling, S.; Askari, E. A meshfree method based on the peridynamic model of solid mechanics. *Comput. Struct.* **2005**, *83* (17-18), 1526–1535.

33. Silling, S. A.; Epton, M.; Weckner, O.; Xu, J.; Askari, E. Peridynamic states and constitutive modeling. *J. Elasticity* **2007**, *88* (2), 151–184.

34. Berenger, J. A perfectly matched layer for the absorption of electromagnetic-waves. *J. Comput. Phys.* **1994**, *114* (2), 185–200.

35. Chew, W.; Weedon, W. A 3D perfectly matched medium from modified Maxwell's equations with stretched coordinates. *Microw. Opt. Tech. Lett.* **1994**, *7* (13), 599–604.

36. Wildman, R. A.; Gazonas, G. A. *A perfectly matched layer for peridynamics in one dimension*; ARL-TR-5626; U.S. Army Research Laboratory: Aberdeen Proving Ground, MD, 2011.

37. Du, Q.; Gunzburger, M. D.; Lehoucq, R. B.; Zhou, K. *A nonlocal vector calculus, nonlocal volume-constrained problems, and nonlocal balance laws*; SAND 2010-8353J; Sandia National Laboratories: Sandia, NM, 2010.

38. Malvern, L. *Introduction to the Mechanics of a Continuous Medium;* Prentice-Hall: NJ, 1969.

39. Foster, J. T.; Silling, S. A.; Chen, W. W. Viscoplasticity using peridynamics. *Int. J. Numer. Meth. Eng.* **2010**, *81*, 1242–1258.

40. Johnson, S. G. Notes on Perfectly Matched Layers. http://math.mit.edu/~stevenj/18.369/pml.pdf, (accessed 2010).

List of Symbols, Abbreviations, and Acronyms

1-D	one-dimensional
2-D	two-dimensional
α-SiO_2	crystalline quartz
Al	aluminum
$AlON$	aluminum oxynitride
ARL	U.S. Army Research Laboratory
a-SiO_2	fused silica or amorphous quartz
BKS	MD potential named after authors (*9*)
B	boron
Ca	calcium
CSM	continuous stiffness measurement
DAC	diamond anvil cell
DSI	Director's Strategic Initiative
EOI	edge-on-impact
EOS	equation of state
FEM	finite element method
FIB	focused-ion-beam
HEL	Hugoniot elastic limit
IRO	intermediate-range order
LAMMPS	large-scale atomic/molecular massively parallel simulator
LB	less brittle
MD	molecular dynamics
Na	sodium
MEDE	materials in extreme dynamic environments
NVT	constant volume-constant temperature
O	oxygen
PAW	projector augmented wave
PML	perfectly matched layer
RDF	radial distribution function
SAXS	small-angle x-ray scattering
SCJ	shaped-charge jet
SEET	strain energy equivalence theory
SEM	scanning electron microscopy

List of Symbols, Abbreviations, and Acronyms (Continued)

Si	silicon
SiC	silicon carbide
SL	soda lime
SRO	short-range order
STEM	scanning tunneling electron microscopy
VASP	Vienna ab initio simulation package
WMRD	Weapons and Materials Research Directorate

NO. OF COPIES	ORGANIZATION
1 (PDF ONLY)	DEFENSE TECHNICAL INFORMATION CTR DTIC OCA 8725 JOHN J KINGMAN RD STE 0944 FORT BELVOIR VA 22060-6218
1	DIRECTOR US ARMY RESEARCH LAB IMNE ALC HRR 2800 POWDER MILL RD ADELPHI MD 20783-1197
1	DIRECTOR US ARMY RESEARCH LAB RDRL CIO LL 2800 POWDER MILL RD ADELPHI MD 20783-1197
1	DIRECTOR US ARMY RESEARCH LAB RDRL CIO MT 2800 POWDER MILL RD ADELPHI MD 20783-1197
1	DIRECTOR US ARMY RESEARCH LAB RDRL D 2800 POWDER MILL RD ADELPHI MD 20783-1197

NO. OF COPIES	ORGANIZATION
2	NSF S MCKNIGHT G PAULINO 4201 WILSON BLVD, STE 545 ARLINGTON, VA, 22230-0002
2	DARPA W COBLENZ J GOLDWASSER 3701 N FAIRFAX DR ARLINGTON VA 22203-1714
1	DIRECTOR US ARMY ARDEC AMSRD AAR AEE W E BAKER BLDG 3022 PICATINNY ARSENAL NJ 07806-5000
1	COMMANDER US ARMY RSRCH OFC RDRL ROE M D STEPP PO BOX 12211 RESEARCH TRIANGLE PARK NC 27709-2211
1	RUTGERS UNIVERSITY DEPT MATLS SCI & ENGRG R LEHMAN 607 TAYLOR ROAD PISCATAWAY, NJ 08854
1	CLEMSON UNIV DEPT OF MECH ENGRG M GRUJICIC 241 ENGRG INNOVATION BLDG CLEMSON SC 29634-0921
1	UNIVERSITY OF MISSISSIPPI DEPT OF MECH ENGRG A M RAJENDRAN 201-B CARRIER HALL UNIVERSITY, MS 38677
2	SRI INTERNATIONAL D CURRAN D SHOCKEY 333 RAVENSWOOD AVE MENLO PARK CA 94025

NO. OF COPIES	ORGANIZATION
1	INST OF ADVANCED TECH UNIV OF TX AUSTIN S BLESS 3925 W BRAKER LN STE 400 AUSTIN TX 78759-5316
5	SOUTHWEST RSRCH INST C ANDERSON K DANNEMANN T HOLMQUIST G JOHNSON J WALKER PO DRAWER 28510 SAN ANTONIO TX 78284
1	APPLIED RSCH ASSOCIATES D E GRADY 4300 SAN MATEO BLVD NE STE A220 ALBUQUERQUE NM 87110
2	WASHINGTON ST UNIV INST OF SHOCK PHYSICS Y M GUPTA J ASAY PULLMAN WA 99164-2814
1	JOHNS HOPKINS UNIV DEPT OF MECH ENGRG K T RAMESH LATROBE 122 BALTIMORE MD 21218
1	UNIV OF TEXAS-PAN AMERICAN COLLEGE OF ENGRG & COMPUTER SCI D H ALLEN 1201 WEST UNIVERSITY DR EDINBURG, TX 78539-2999
1	UNIV OF DAYTON RSRCH INST N S BRAR 300 COLLEGE PARK MS SPC 1911 DAYTON OH 45469

NO. OF COPIES ORGANIZATION

4 RDRL D
C CHABALOWSKI
J CHANG
O OCHOA
R SKAGGS
BLDG 205
2800 POWDER MILL RD
ADELPHI MD 20783-1197

ABERDEEN PROVING GROUND

86 DIR USARL
RDRL WM
B FORCH
S KARNA
J MCCAULEY
P PLOSTINS
P BAKER
RDRL WML
J NEWILL
M ZOLTOSKI
RDRL WML B
I BATYREV
S IZVYEKOV
B RICE
R PESCE RODRIGUEZ
D TAYLOR
N TRIVEDI
N WEINGARTEN
RDRL WML D
P CONROY
M NUSCA
RDRL WML E
P WEINACHT
RDRL WML F
D LYON
RDRL WML G
M BERMAN
W DRYSDALE
RDRL WML H
D SCHEFFLER
S SCHRAML
B SCHUSTER
RDRL WMM
J BEATTY
R DOWDING
J ZABINSKI
RDRL WMM A
J TZENG
E WETZEL
RDRL WMM B
T BOGETTI
B CHEESEMAN
C FOUNTZOULAS
G GAZONAS
D HOPKINS
R KARKKAINEN
B LOVE
P MOY
B POWERS
C RANDOW
T SANO
F TAVAZZA
M VANLANDINGHAM
R WILDMAN
C YEN
RDRL WMM C
J LA SCALA
RDRL WMM D
E CHIN
K CHO
RDRL WMM E
J ADAMS
M COLE
T JESSEN
J LASALVIA
P PATEL
J SANDS
J SINGH
RDRL WMM F
L KECSKES
H MAUPIN
RDRL WML G
J ANDZELM
A RAWLETT
RDRL WMP
B RINGERS
S SCHOENFELD
RDRL WMP B
M GREENFIELD
C HOPPEL
R KRAFT
M SCHEIDLER
T WEERASOORIYA
RDRL WMP C
R BECKER
S BILYK
T BJERKE
D CASEM
J CLAYTON
B LEAVY
M RAFTENBERG

NO. OF COPIES	ORGANIZATION
	S SATAPATHY
	S SEGLETES
	RDRL WMP D
	R DONEY
	D KLEPONIS
	J RUNYEON
	B SCOTT
	H MEYER
	RDRL WMP E
	M BURKINS
	RDRL WMP F
	A FRYDMAN
	N GNIAZDOWSKI
	R GUPTA
	RDRL WMP G
	N ELDREDGE
	D KOOKER
	S KUKUCK
	G R PEHRSON

NO. OF COPIES	ORGANIZATION